Optics and Lasers in Engineering 172 (2024) 107885

Contents lists available at ScienceDirect

Optics and Lasers in Engineering

journal homepage: www.elsevier.com/locate/optlaseng

Vision-based detection and coordinate metrology of a spatially encoded multi-sphere artefact

Mohammed A Isa [a,*], Richard Leach [a], David Branson [a,b], Samanta Piano [a]

[a] Manufacturing Metrology Team, Faculty of Engineering, University of Nottingham, Nottingham, United Kingdom
[b] Nottingham Advanced Robotics Laboratory, Faculty of Engineering, University of Nottingham, Nottingham, United Kingdom

ARTICLE INFO

Keywords:
Vision
Detection
Metrology
Coordinate measurement
Heteroscedasticity
Photogrammetry
Sphere
Binocular
Trinocular
Edge spread

ABSTRACT

New developments in vision algorithms prioritise identification and perception over accurate coordinate measurement due to the complex problem of resolving object form and pose from images. Consequently, many vision algorithms for coordinate measurements rely on known targets of primitive forms that are typically planar targets with coded patterns placed in the field of view of vision systems. Although planar targets are commonly used, they have some drawbacks, including calibration difficulties, limited viewing angles, and increased localisation uncertainties. While traditional tactile coordinate measurement systems (CMSs) adopt spherical targets as the de facto artefacts for calibration and 3D registration, the use of spheres in vision systems is limited to occasional performance verification tasks. Despite being simple to calibrate and not having orientation-dependant limitations, sphere targets are infrequently used for vision-based in-situ coordinate metrology due to the lack of efficient multi-view vision algorithms for accurate sphere measurements. Here, we propose an edge-based vision measurement system that uses a multi-sphere artefact and new measurement models to extract sphere information and derive 3D coordinate measurements. Using a spatially encoded sphere identities embedded in the artefact, a sphere matching algorithm is developed to support pose determination and tracking. The proposed algorithms are evaluated for robustness, measurement quality and computational speed to assess their performance. At the range of 500 mm to 750 mm, sphere size errors of less than 25 μm and sphere-to-sphere length errors of less than 100 μm are achievable. In addition, the proposed algorithms are shown to improve robustness by up to a factor of four and boost computational speed.

1. Introduction

Advances in optical sensing and computing technologies have improved the resolution and speed of machine vision (MV) technologies [1]. The quality of information conveyed by vision systems has also improved, paving the way for the adoption of MV as a fundamental technology in the advanced manufacturing paradigm of industry 4.0 [2–4]. Previously time-consuming and complex measurement verification processes can now be automated and integrated into industry 4.0 information architectures [5,6]. However, it is necessary to ensure that new strategies in the automated measurement and data management processes remain compliant with existing measurement verification standards. Carrying out detailed in-process measurements using MV that is industrially reliable and supports measurement quality verification remains a major challenge [7]. Commonly, industrial in-process applications limit the functionalities of MV to visual feedback to human operators, identification of tags, monitoring of faults in production lines and so forth [3,8]. The outputs of these applications are typically data-driven simplified logical or numerical values, which inform process control and monitoring [9,10]. The problem with these simplified outputs is that without rigorous metrological assessment, it becomes difficult to determine the reliability of the conveyed information. If the outputs of MV systems can be related to physical coordinates of known calibrated targets, it is possible to assess known dimensions and establish metrological traceability through the calibrated reference measurements of the targets [11,12]. Therefore, through the coordinate measurements of integrated dimensional artefacts, the associated uncertainties of MV measurements can be evaluated in-line.

MV technologies and algorithms enable the use of cameras for carrying out vision-based measurements in industrial environments. Driven by the desire to automate inspection, improve quality and reduce cost [13], vision-based measurement has progressed to become a core

* Corresponding author.
E-mail address: mohammed.isa@nottingham.ac.uk (M.A. Isa).

https://doi.org/10.1016/j.optlaseng.2023.107885
Received 3 June 2023; Accepted 6 October 2023
Available online 11 October 2023

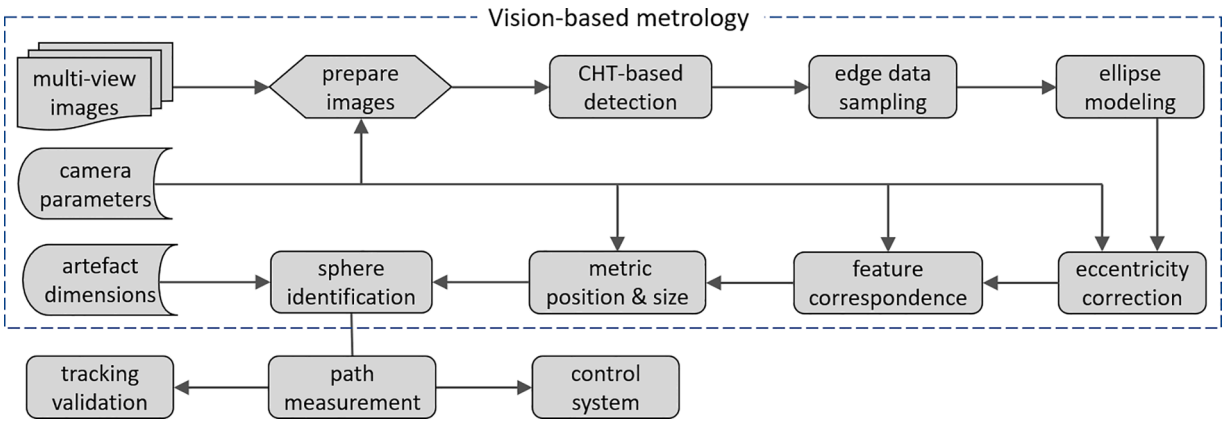

Fig. 1. Processes involved in the vision-based artefact detection, coordinate measurement and identification.

technology in intelligent manufacturing industries [2,6]. At the centre of vision-based measurement systems is the projective mapping of 3D geometric shapes to 2D images where depth information is lost. Resolving shapes from image projections is a challenging problem; therefore, common MV strategies rely on either the use of primitive targets or the integration of additional active or passive visual cues [14]. The use of supplementary visual cues, such as speckles [15], fringes [16], silhouettes [17] and structured lights [18], is common for post-process measurements of objects. However, for in-situ determination of the coordinate positions of machine tools and objects, targets of basic geometries are usually placed in the measured area [19–21]. The types of geometric features used as targets are usually limited to point and planar features with limited visibility and difficult-to-calibrate features [22,23]. To estimate measurement quality using targets, we suggest adoption of some processes outlined in standard performance verification documents (ISO 10,360 and VDI/VDE 2634 [24,25]) in real-time vision-based measurements. The use of artefacts made up of spheres, as suggested by these standard documents, can enable maximum visibility, simple target calibration and adoption of quality verification procedures [26,27].

Measurements from vision systems rely on algorithms for detection and extraction of relevant features from images. The general paradigm of feature extraction is aimed at target description and classification for the purpose of recognition, rather than 3D coordinate measurement [28]. Therefore, fast sphere detection algorithms, such as the Hough transformation, centroid operator and blob detection are not accurate and robust enough for coordinate metrology [29,30]. Negative effects of noise, environmental disturbances and eccentricity errors in sphere images must be ameliorated by detection algorithms to maintain consistently high-quality measurements. The majority of vision algorithms depend on low-level features, such as edges, to detect and localise desired features [28], where the statistical dispersion of spread functions in fitting methods assume uniform variance (homoscedasticity) for the features. Due to varying lighting, shadowing and other environmental conditions, image contrast is not uniform and the spread functions of features can be heteroscedastic. Therefore, feature models should take into account the heteroscedasticity of the underlying edge data for improved localisation and specificity [16]. Ellipse-based contour methods using a direct algebraic ellipse model is suggested in reference [31] and ellipse eccentricity errors are simulated in reference [29]. The geometric ellipse models in reference [32] are shown to be more robust than the direct algebraic ellipse model and sigmoidal edge spread functions are used to improve localisation of image edges [33–35]. Essentially, accurate vision-based measurement of spherical feature positions and sizes from images requires solving complex equations and measurement uncertainty is not readily evaluated [36,37]. Research work on vision-based strategies combining accurate feature detection, identification and verification methods for coordinate measurements of sphere-based artefacts is lacking.

Beyond position measurement, orientated coded targets are used to measure the pose of objects and machine tools [38]. In various applications that require digital replication or monitoring of the physical environment, it is necessary to not only measure target positions but also identify the targets along with their orientations [39]. Whenever multiple targets are involved, reliably distinguishing unmarked targets can be a challenging problem. A method of encoding geometric distances between targets to aid target identification was suggested for hand-held collaborative virtual reality applications [40]. Identification tests of the distance-encoded targets indicated that the approach mislabels targets and requires more stability against occlusion. Multi-target artefacts, consisting of a five-sphere frame [41] and light pipes [42], have been suggested to aid measurement of robotic poses where improved coordinate measurement accuracy remains a challenge. For multi-sphere artefacts, we suggest encoding both sphere size and adjacent distances to reinforce sphere target identification process that leads to reliable pose measurement of the artefact.

Combining vision-based 3D coordinate measurements with built-in joint-angle-based measurements has been shown to be an effective way of improving robot positioning accuracy [43–45]. Vision systems provide reference measurements from which the absolute positions of robots can be determined in relation to other objects and systems that interact with robots [46]. These vision systems allow for the intelligent goal-orientated supervisory control of industrial operations that can ensure quality and efficiency [47]. Simultaneous quality assessment of measured positions can be accomplished by using the proposed spatially encoded artefact that is pre-calibrated. The calibrated dimensions of the artefact can support both the identification of features and the evaluation of measurement quality.

Vision-based coordinate metrology comprises prerequisite processes that include vision system characterisation [48], feature recognition [49], modelling of image data [26], finding correspondence from multi-view features [50] and metric reconstruction [51,52] (see reference [53] for a review of optical coordinate metrology). These processes cover multiple areas of research and collectively affect the quality of measurements. To introduce and investigate new contributions in the different stages of coordinate measurement using a sphere-based measurement artefact, we propose a measurement scheme that synthesises the various prerequisite processes. We propose methods ranging from image-based detection and localisation strategies to dimension and coordinate measurements. The novelty in the paper is outlined through improvements of existing methodologies by revision and derivation of measurement models, error reduction strategies for feature extraction and implementation of 3D feature identification through the spatial encoding of the measurement artefact. This paper contributes to various applications where physical environments are monitored by accurate measurement of positions and poses of objects such as robotic arms,

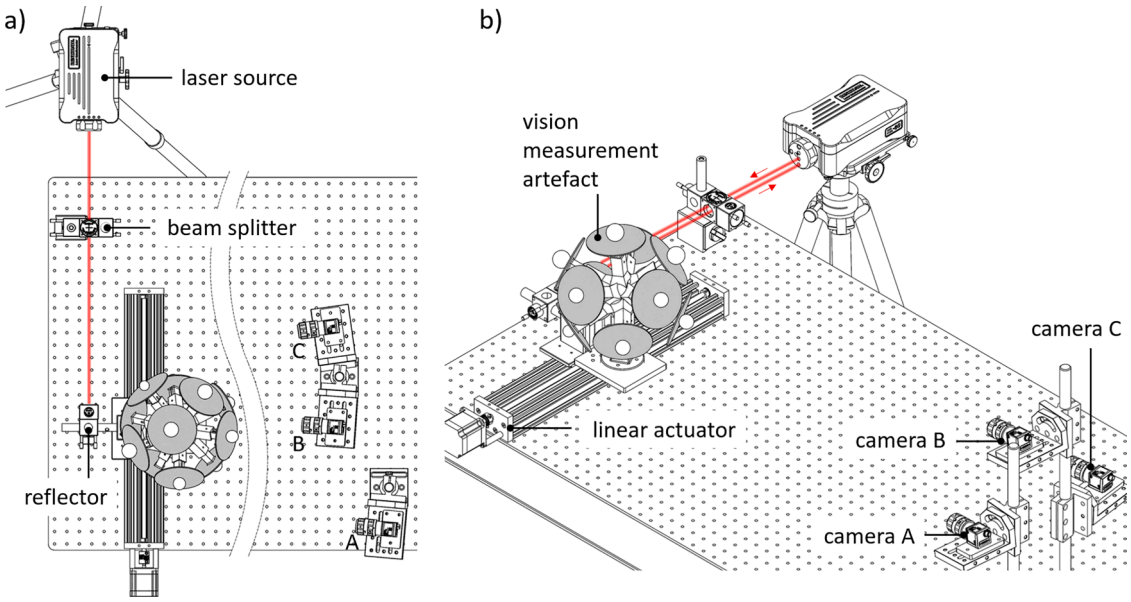

Fig. 2. Experimental setup of a vision system and a laser interferometer for the measurement of artefact position and size; a) shows the top view and b) shows the isometric view of the setup.

virtual reality equipment and manufactured products [54]. Here, the measurement artefact structure can be tailored into a size and shape that fits a specific application.

In Section 2 of this paper, we explain the setup of the measurement test and the proposed measurement methodology from image localisation of target features to 3D coordinate and size measurements of the identified targets. The performance of the proposed image localisation models and coordinate measurement methods are discussed in Section 3. The performance results are investigated in terms of measurement quality, computational complexity and robustness. After conclusion of the paper in Section 4, additional information referenced in the paper are presented in the supplementary sections—Supplementary material, Appendix A and Appendix B.

2. Detection and measurement methodology

This section describes the components and processes involved in measuring spherical features of a vision-based measurement artefact. First, the experimental setup is introduced, followed by the detailed strategies employed for feature identification, localisation and coordinate measurement. We also discuss methods for reducing errors and improving the accuracy of photometric feature measurements, as well as the derivation of explicit solutions for the metric 3D measurements using both binocular and trinocular vision systems. Additionally, a graph-matching approach for sphere identification from images of the artefact at different positions is presented. Fig. 1 provides an overview of the vision-based coordinate measurement system (CMS).

Beginning with captured multi-view images, known camera parameters and artefact dimensions as indicated in Fig. 1, a circular Hough transform (CHT) algorithm is used for determining the regions of interest (ROIs) where spheres are recognised in images. Edge points are then sampled, modelled and eccentricity errors in all detected image features are estimated and compensated. Using the feature correspondence of detected images from different camera views, the metric 3D position and size of the spherical features are evaluated. Finally, known pre-calibrated artefact dimensions are used to determine the identity of every measured sphere feature.

2.1. Experiment

Three 20 mega-pixel Basler machine vision cameras, each with a 16 mm focal length, were used to capture three sets of multi-view images in this paper. The three cameras were pre-calibrated as binocular camera pairs AB, AC, and BC (as shown in Fig. 2) using MATLAB's computer vision toolbox, at distances ranging from 500 mm to 750 mm. The pre-calibration process uses a 200 mm by 150 mm checkerboard artefact fabricated by lithographic printing with square sizes of 15 mm, manufactured with a tolerance of 20 μm. The obtained binocular camera parameters were used to characterise the trinocular vision system consisting of the three cameras using the method described elsewhere [55]. The pre-calibration process estimated the cameras' intrinsic parameters (the pixel focal lengths, principal point location and lens distortion coefficients) as well as inter-camera properties, such as relative camera positions and orientations. Radial distortions of the binocular and trinocular camera systems were expressed using three and six distortion coefficients respectively, while tangential distortion was considered negligible [55]. For every reference to image point, it is assumed that image distortions have been corrected using the distortion model described in Section 2.5.1.

The measurement artefact used in this paper is made up of eleven white polyoxymethylene solid spheres attached to dark contrasting plates (shown in Fig. 2). To ensure that the identity of every sphere could be determined from any camera pose, the diameter and spacing of the spheres were designed to encode sphere identities. Specifically, the artefact was designed to guarantee the following conditions:

1 at least three spheres are visible at any configuration of the artefact,
2 the nominal diameters and distances between neighbouring spheres are selected from the candidate sets $\mathscr{D} = \{20, 25, 30\}$ mm and $\mathscr{L} = \{107, 114, 121, 128, 135, 142\}$ mm respectively, and
3 every group of three neighbouring spheres has a unique set of diameter and spacing arrangement.

To facilitate the experimental tests, the measurement artefact was securely fastened to a linear actuator stage depicted in Fig. 2 after artefact calibration using a Mitutoyo Crysta Apex S7106 contact CMS with a stylus of 2 mm diameter. With travel range of 300 mm, the actuator also carries the reflector for a distance measuring Renishaw XL-

Table 1
Diameters of vision artefact spheres showing the diameter values as designed and as calibrated.

Sphere index (n_a)	Design /mm	Calibrated ($\mathscr{S}_a$) /mm	Uncertainty /μm
2	25	24.988	2
3	30	29.999	2
4	20	19.973	3
5	30	29.990	3
6	30	29.981	3
7	30	29.975	4
8	20	19.961	3
9	25	24.969	2
10	25	24.984	3
11	25	24.990	4
12	20	19.966	3

Table 2
As-designed and as-calibrated distances between adjacent spheres.

Adjacent sphere pairs	Design /mm	Calibrated ($\mathscr{E}_a$) /mm	Uncertainty /μm
2–3	121	121.870	8
2–7	114	114.725	7
2–9	107	108.223	9
2–11	128	129.173	12
3–7	142	142.910	8
3–8	107	108.027	13
3–12	114	115.081	11
4–5	121	121.163	7
4–10	121	121.101	8
4–11	121	120.742	9
4–12	121	121.437	8
5–6	121	121.289	7
5–8	135	134.702	1
5–10	121	121.299	3
5–12	121	120.363	9
6–7	114	114.647	9
6–8	135	134.643	3
6–9	142	142.336	7
6–10	128	128.231	4
7–8	128	128.795	8
7–9	107	107.797	9
8–12	114	114.353	12
9–10	142	141.928	9
9–11	107	107.956	7
10–11	121	120.969	10

80 laser interferometer, which has a certified measurement accuracy of $\pm$ 0.3 μm for the distances measured in this paper. The actuator is responsible for moving the artefact and reflector when the artefact is measured by the cameras and laser interferometer.

Table 1 lists the calibrated diameters of the artefact spheres, determined by measuring twenty-five points on each sphere's surface with the Mitutoyo contact CMS. Each sphere is indexed and sphere the indices are used for the expression of sphere adjacency. In Table 2, the distances between adjacent spheres of the artefact, calibrated by the contact CMS, are also listed. Sphere index pairs represent all the adjacent spheres of the artefact. The combination of the sphere adjacency, sizes $\mathscr{S}_a$ and spacings $\mathscr{E}_a$ fully define the geometric structure of the artefact. The expanded uncertainties in the tables are expressed at confidence intervals of 95 % from three repeats of sphere diameter and centre coordinate measurements using the contact CMS.

2.2. Image feature recognition

Image features contain specific properties that are both detectable and desirable for implementation in MV algorithms. Recognition of such features is commonly the starting point of computer and MV algorithms. For an image of the spherical targets in this paper, we observe corresponding image features that represent the projections of sphere silhouettes viewed from the image's camera centre. The properties of the image feature depend on the sphere size and its relative location with respect to the camera. Viewed from a camera, the observable contour of a sphere is a tangential circle on the sphere that has a diameter less than the diameter of the sphere. The projection of the sphere contour is an ellipse, which serves as the image feature for the sphere [56].

Given an image containing ellipse features, the aim of a feature recognition process is to determine approximately where the features are located in the image. This paper implements CHT for the recognition of the desired image features. The CHT algorithm searches for images points that are close to the boundaries of circles of a given radial range using convolution or Hough transform filtering [57]. The algorithm is robust and sensitive enough for MV applications with circular and elliptical features [58].

In this paper, CHT is implemented on images where resolution is downscaled for two reasons. First, there is no need for a high-resolution search of image points as the features are elliptical and not exactly circular. Therefore, CHT detection is only used to obtain approximate information about the location and size of the features. Accurate localisation of features is carried out afterwards in segmented ROIs of every identified image feature. It was observed that for all spheres in this paper, where diameters are less than 50 mm and distances greater than 500 mm from all cameras, CHT can recognise image features easily because the eccentricity values of the corresponding image ellipses are small. The second reason for using downscaled images is to improve the speed and efficiency of the CHT implementation. Compared to full-scale images where CHT computation takes up to 4 s, images downscaled by a factor of eight take less than 0.2 s to search. Furthermore, it was observed that the downscaled images have the added benefit of recognising more candidate image ROIs at a given CHT sensitivity.

The CHT recognition algorithm covered in this section provides critical information about where more demanding computations should be carried out to accurately characterise the elliptical image features. To reduce the computational cost of searching for circular features using the Hough transform, the implemented CHT algorithm breaks down the search into multiple sub-problems that focus on specific ranges of search radii. By doing so, we can avoid the computationally expensive search operations that would be required if we were to perform a single CHT search over a wide range of radii.

2.3. Gradient-based edge localisation

From the candidate image features identified in Section 2.2, up to a maximum of eight features with the highest detection metrics per image are selected for a more accurate localisation process. The estimated location and size of each candidate feature are used to determine a rectangular ROI for a high-resolution determination of the feature edge. To accurately estimate edges, edge points are sampled close to the resolution limit of the camera using a gradient-based method similar to ISO 12,233 edge localisation methodology [59]. Essentially, a detailed vision system response to a sphere contour is investigated using the sampled image intensity around the edge of the image feature corresponding to the sphere contour.

Fig. 3a) shows a feature ROI where edge profile sections are probed at different values of the parameterisation angle $\phi_i \in (0, 2\pi]$, where the arc spacing of the probed sections are roughly four to five pixels. Intensity values, known as edge spread functions (ESFs) [59], along the edge profile sections, are evaluated by bilinear interpolation of the image pixel intensities. As shown in Fig. 3b), the ESF declines sharply in the vicinity of the feature edge and this intensity reduction is useful in the determination of the edge location. When the ESF is negated ($-y_{ESF}$) and the first derivative $\left(y_{LSF} = \frac{-dy_{ESF}}{dr_p}\right)$ is taken along the profile distance r_p, the line spread function (LSF), shown in Fig. 3c) is obtained. The LSF is the gradient of the edge profile and gradients are essential for edge detection. Using the LSF, the edge localisation problem is translated to the evaluation of the peak position of the LSF. The ESF and LSF data are

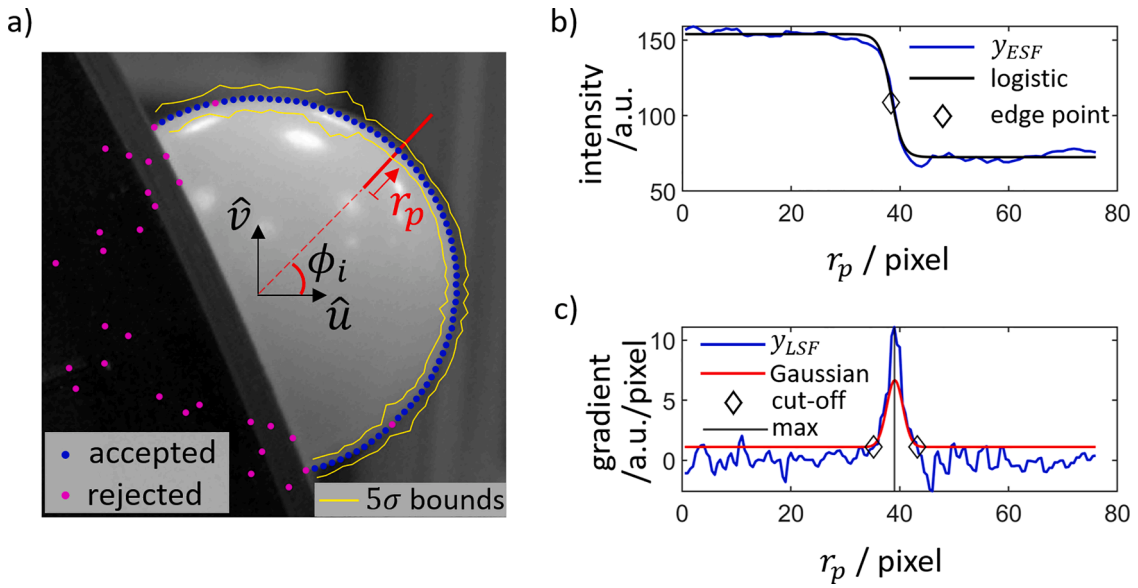

Fig. 3. Edge point localisation showing: a) a cross-sectional line of a sampled edge profile and edge points that are accepted and rejected at various profile positions along with the five-sigma bounds of the line spread function (LSF) of the edge points, b) the edge spread function (ESF) and the logistic-fitted model of the sampled edge profile, and c) the LSF of the sampled profile, maximum gradient edge location and Gaussian-fitted model.

not commonly smooth and the edge location is affected by noise in the image. ISO 12,233 suggests applying a hamming window filter to the LSF, before evaluating edge location, to reduce the influence of noise [33]. A simple method of determining the edge location is by directly extracting the pixel location of the maximum value of the LSF. However, the evaluated location resolution is limited by the sampling rate of the probed profile which makes continuous sub-pixel localisation impossible. A more precise localisation can be estimated using the gradient-weighted centroid of the LSF.

While a high degree of smoothing of the sampled edge spread data can suppress noise, it can also lead to over-averaging and loss of high-spatial frequency information that defines edge location at high resolution. As an alternative, there are known analytical models that can fit the ESF and LSF data to reduce the effect of noise [35]. Observing the ESF in Fig. 3b), $-y_{ESF}$ has the characteristic "S" shape of sigmoidal functions. Fitting the edge spread data to sigmoidal functions can optimise edge location by refining the intensity distribution at the edge. Two sigmoidal functions—logistic and Gaussian error functions—are investigated for modelling edge spread data in this paper.

One common sigmoidal function for modelling ESFs is the logistic function [35,34]. For the edge profile, shown in Fig. 3a), probed at the angle ϕ_i with ESF values of $\boldsymbol{y}_{ESF}$, sampled along the radial profile distances of $\boldsymbol{r}_p$, the ESF data $(\boldsymbol{r}_p,\ \boldsymbol{y}_{ESF})$ is fitted to $(\boldsymbol{x}, \boldsymbol{f}_h(\boldsymbol{x}))$ for the logistic function given by

$$\boldsymbol{f}_h(\boldsymbol{x}) = \frac{y_h}{1 + e^{-\frac{(\boldsymbol{x}-\mu_h)}{s_h}}} + d_h, \tag{1}$$

where y_h and d_h are the height scale and offset parameters respectively. The distribution scale parameter is s_h, while μ_h is the distribution location parameter of the logistic function. The best-fit solution for the four parameters given the ESF data is outlined in Appendix A.1. Fig. 3b) shows the fitted logistic plot of the ESF data and the edge point location derived from the logistic function in Eq. (1).

The second sigmoidal function considered for modelling edge spread data is the Gaussian error function. When the ESF of a probed edge profile $(-y_{ESF})$ is designated as a Gaussian error function, the LSF, which is the gradient of the ESF, takes the form of a Gaussian function—the probability distribution function (PDF) of the Gaussian error function. Here, LSF data $(\boldsymbol{r}_p,\ \boldsymbol{y}_{LSF})$ is fitted to $(\boldsymbol{x}, \boldsymbol{f}_g(\boldsymbol{x}))$ for the Gaussian function given by

$$\boldsymbol{f}_g(\boldsymbol{x}) = y_0 e^{-\frac{(\boldsymbol{x}-\mu)^2}{2\sigma_r{}^2}}, \tag{2}$$

where the Gaussian mean μ, standard deviation σ_r and height y_0 parameters need to be determined. The Gaussian fitting problem seeks to find the values of these parameters that minimise the difference between the LSF data $(\boldsymbol{r}_p,\ \boldsymbol{y}_{LSF})$ and the ideal Gaussian values $(\boldsymbol{x}, \boldsymbol{f}_g(\boldsymbol{x}))$. To avoid computationally expensive iterations, the Gaussian function can be linearised by exploiting the fact that Eq. (2) is an exponential function of a quadratic function. Therefore, a proposed Caruana Gaussian fitting algorithm [60] reduces the Gaussian fitting problem to a linear problem by expressing Eq. (2) in the logarithmic scale. Appendix A.2 explains the linear least-squares approach used to solve the Gaussian fitting problem in this paper.

As can be observed in Fig. 3c), the signal-to-noise ratio (SNR) of the curve $\boldsymbol{y}_{LSF}$ increases as the gradient value (y_{LSF}) diminishes at the two tails of the curve. The noise at the tails of $\boldsymbol{y}_{LSF}$ significantly impacts the result of the Caruana Gaussian fitting process [61]. As a result, the gradient cut-off points, shown in Fig. 3c), are suggested to ensure only high gradient data between the cut-off points is fitted to the Gaussian model. Furthermore, a gradient-weighted Caruana algorithm [61], which reduces the sensitivity of Gaussian fitting to noise, is also implemented. Details on the implementation of the weighted Caruana algorithm are provided in Appendix A.2. It should be noted that the use of edge profile cut-off points is only implemented to the Gaussian models and not the aforementioned logistic function because the logistic fitting algorithms fails occasionally when edge profile data is reduced to the profile length between the cut-off points.

Apart from image noise, the probed edge profile could also contain erroneous edges that do not belong to the desired feature. It is also possible for parts of the desired feature to have weak edges or be occluded; hence, the probed profile at those edge profiles should be discarded. To mitigate erroneous points from being considered as part of the feature edges, the following selection criteria are implemented when the edge points are probed:

- gradient strength: the gradient must be greater than a threshold gradient value;

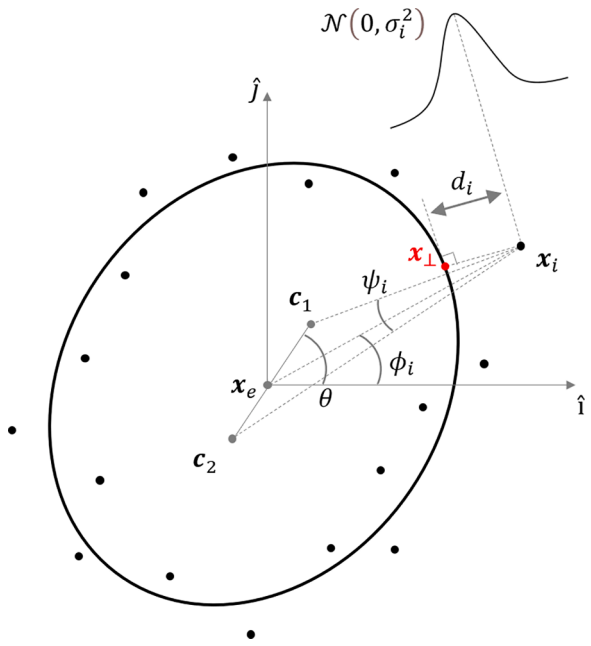

Fig. 4. Illustration of an ellipse fitted to data points showing the orthogonal distance d_i of the point $\boldsymbol{x}_i$ from the ellipse, foci $(\boldsymbol{c}_1, \boldsymbol{c}_2)$, ellipse centre $\boldsymbol{x}_e$, ellipse major axis angle θ and the normally distributed $\mathcal{N}(0, \sigma_i^2)$ line spread function of the edge point $\boldsymbol{x}_i$.

- radial consistency: the change in radial distance from the probed feature centre must be less than a radial distance threshold;
- tangential consistency: the change in the angle between the tangential and radial directions must not exceed a tangential angle threshold;
- second derivative agreement: the zero-crossing of the ESF second derivative $\left(\frac{-dy_{ESF}^2}{d^2 r_p} = 0\right)$ must be located near the edge point.

The above criteria are checked simultaneously as the edge points are probed, and the selection operation takes only (8 ± 0.5) ms per image, where each image contains six to eight spherical features. The edge point selection method is fast and efficiently improves the quality of the probed data by accepting only points that are compliant with the four criteria given above. Fig. 3a) shows the accepted points that pass the selection criteria, indicating how effective the selection criteria are at rejecting erroneous edge points. The quantitative evaluation of the performance and computational complexity of the investigated edge localisation strategies are discussed in Section 3.

2.4. Image feature models

Simply sampling edge points alone does not convey important information on the size and location of the image features; they need to be fitted to the expected shape of the features. Based on the geometric setup between the spheres and image planes used, the projection of the 3D circular spherical contours on the image planes results in elliptical type of conic sections. When we consider the cone of light emanating from a sphere and terminating at the camera centre (a cone vertex), the image plane intersection with the surface of the cone of light is an ellipse. Therefore, the sampled edge points belong to ellipse features and should be fitted accordingly to elliptical models.

A two-dimensional (2D) ellipse is fully defined by five parameters, and in parametric form, they are two location parameters, two size parameters and one orientation parameter. When an ellipse is instead represented as a general conic, six parameters in the form of algebraic coefficients are used, but these coefficients should be subject to an ellipticity constraint. Fitting an ellipse to given data points involves minimising error measures between the data and the model ellipse. In this paper, we distinguish the ellipse fitting models by the type of error measure implemented by the model.

The first ellipse model considered in this paper is the direct ellipse fitting model that uses constrained algebraic conic parameters to minimise algebraic distance [31]. This direct model is fast but lacks the necessary geometric interpretation of the minimised distance and optimised parameters, thereby limiting the ability to associate geometric uncertainty to the outcome. The computational details of the direct model are given elsewhere [31]. Serving as the elementary ellipse model, the direct ellipse model is implemented as a computational starting point and for comparison with other ellipse fitting models that improve the direct model.

In addition to the direct algebraic model, we also investigate two geometric ellipse fitting models. The first geometric model implemented is the orthogonal-distance geometric (ODG) model, where the deviations of edge points are evaluated as the closest orthogonal distances to an ellipse. The five ellipse parameters ($\boldsymbol{\Omega} = [\mathrm{a},\ \mathrm{b}, u_e, \mathrm{v_e}, \theta]$) solved by the ODG method are the standard parametric ellipse parameters: the semi-major axis length a, the semi-minor axis length b, the ellipse centre components $\boldsymbol{x}_e(u_e, v_e)$ and the ellipse angle θ. For each edge point $\boldsymbol{x}_i$, the nearest orthogonal point on the ellipse $\boldsymbol{x}_\perp$ is required to minimise the following ODG objection function

$$\min_{\boldsymbol{\Omega}} \frac{1}{n} \sum_{i=1}^{n} f_{ODG}(\boldsymbol{\Omega}) = \min_{\boldsymbol{\Omega}} \frac{1}{n} \sum_{i=1}^{n} \left(\| \overrightarrow{\boldsymbol{x}_\perp \boldsymbol{x}_i} \| \right)^2. \tag{3}$$

Fig. 4 illustrates the ellipse parameters, the location of the orthogonal ellipse point $\boldsymbol{x}_\perp$ and the closest orthogonal distance $d_i = \| \overrightarrow{\boldsymbol{x}_\perp \boldsymbol{x}_i} \|$. A two-level iteration problem is encountered when implementing the objective function; for each iteration of the ellipse parameters $\boldsymbol{\Omega} = [\mathrm{a},\ \mathrm{b},\ u_e, \mathrm{v_e}, \theta]$, the locations of $\boldsymbol{x}_\perp$ must be determined by another iteration. The initial ellipse iteration parameters are obtained by conversion of the six parameters of an elliptical conic, solved by the direct algebraic model, using the expressions given in reference [62].

The second geometric model uses the geometric definition of an ellipse, as the locus of 2D points, with a constant sum of distances from two focal points [32]. These two focal points, referred to as the ellipse foci $(\boldsymbol{c}_1,\ \boldsymbol{c}_2)$, define ellipse location, orientation and linear eccentricity. The ellipse centre $\boldsymbol{x}_e$ lays at the mid-point of the two foci, as shown in Fig. 4. The ellipse's major axis passes through the ellipse foci and centre, as well as the farthest points (ellipse vertices) on the ellipse. The combination of the ellipse focal locations, $\boldsymbol{c}_1(c_{1u}, c_{1v})$ and $\boldsymbol{c}_2(c_{2u}, c_{2v})$, and the length of the ellipse semi-major axis a is sufficient to fully define an ellipse. We represent the combination of the ellipse foci and semi-major length as the foci-based ellipse parameters $\boldsymbol{\Lambda} = [a, c_{1u}, c_{1v}, c_{2u}, c_{2v}]$. For every point sampled on an ellipse, the sum of distances from that point to $\boldsymbol{c}_1$ and $\boldsymbol{c}_2$ has a constant value of $2a$. Based on this constant, the geometric distance error of an arbitrary edge point $\boldsymbol{x}_i$ to the foci is given by $\| \overrightarrow{\boldsymbol{c}_1 \boldsymbol{x}_i} \| + \| \overrightarrow{\boldsymbol{c}_2 \boldsymbol{x}_i} \| - 2a$. By further normalisation of this distance error [32], the foci-based geometric (FBG) approach minimises the sum of the squared error of foci-based distances of n edge points given by

$$\min_{\boldsymbol{\Lambda}} \frac{1}{n} \sum_{i=1}^{n} f_{FBG}(\boldsymbol{\Lambda}) = \min_{\boldsymbol{\Lambda}} \frac{1}{n} \sum_{i=1}^{n} \left(\frac{1}{1 + \gamma \cos(\psi_i)} \left(\| \overrightarrow{\boldsymbol{c}_1 \boldsymbol{x}_i} \| + \| \overrightarrow{\boldsymbol{c}_2 \boldsymbol{x}_i} \| - 2a \right)^2 \right), \tag{4}$$

where $\psi_i < \frac{\pi}{2}$ is the angle $\widehat{\boldsymbol{c}_1 \boldsymbol{x}_i \boldsymbol{c}_2}$ (see Fig. 4) and γ is the tuning parameter with a value between zero and one, which can be set using the method outlined in reference [32]. The FBG error function $f_{FBG}(\boldsymbol{\Lambda})$ in Eq. (4) is normalised by the angle-dependant term to account for the non-uniformity of the contribution of the point deviations at different points of the ellipse.

The FBG objective function given in Eq. (4) does not consider the difference in the edge spread of each point and, therefore, assumes the

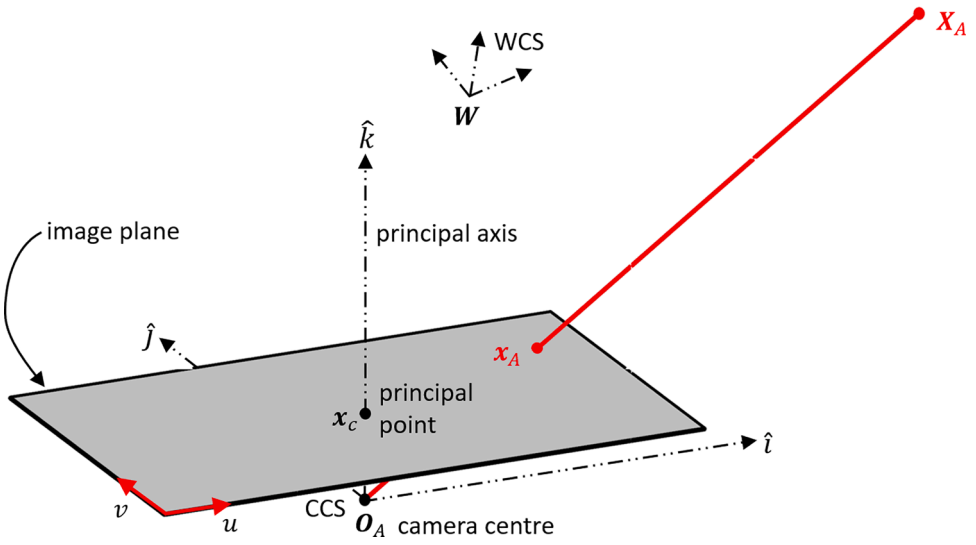

Fig. 5. Projection mapping of a 3D point X_A onto the image plane of camera A showing the camera coordinate system (CCS) and the world coordinate system (WCS).

points have isotropic LSF variances. The edge of an ellipse feature can have varying contrast, sharpness, noise, illumination and background colour. These differences can make the variance of the LSF of some edge points significantly larger than that of others. We revise Eq. (4) to reflect the anisotropic variance of the edge points to improve the ellipse fitting. The distribution of the LSF of the sample sphere edge in Fig. 3a), given by the five-sigma bounds of the LSF Gaussian fitting, shows that the variance varies for edge points.

The contribution of the non-normalised FBG distance error $(\| \overrightarrow{c_1x_i}\| + \|\overrightarrow{c_2x_i}\| - 2a)^2$ of a point, to the expectation of the orthogonal distance error of the same point, is approximately proportional to $\sigma_i^2(1 + \cos(\psi_i))$, assuming the point has normally distributed probability density $\mathcal{N}(0,\sigma_i^2)$, along the nearest orthogonal direction to the ellipse [32]. The method in Section 2.4 already provides the radial variance information for each edge point using the Gaussian or logistic edge localisation methods. For the Gaussian model of the LSF, the radial variance σ_r^2 of the Gaussian-fitted LSF is given directly from Eq. (1). However, a logistic-fitted ESF requires evaluation of the variance from the scale parameter s_h in Eq. (2). The variance of the logistic distribution of the LSF is expressed as $\sigma_r^2 = \frac{\pi^2}{3}s_h^2$ [63].

Let $h = \| \overrightarrow{c_2c_1}\|$ and the ellipse semi-minor axis becomes $b = \sqrt{a^2 - \frac{h^2}{4}}$. The equivalent variance of the probability distribution of the point x_i along the orthogonal distance d_i in Fig. 4 can be estimated by

$$\sigma_i = \sigma_r \frac{ab}{\sqrt{b^2sin^2(\phi) + a^2\cos^2(\phi)}\sqrt{a^2sin^2(\phi) + b^2\cos^2(\phi)}}. \tag{5}$$

For the edge point x_i sampled at the angle ϕ_i in Fig. 4, Eq. (5) is derived from the projection of the radial ellipse-to-point vector on the orthogonal direction vector along d_i. The orthogonal direction vector is simplified as the direction vector perpendicular to the ellipse tangent at the angle ϕ_i. Using the estimated variance for each edge point, the minimisation of a new error function $(f^*_{FBG}(\mathbf{\Lambda}))$ for a heteroscedastic FBG model is obtained as

$$\min_{\mathbf{\Lambda}} \frac{1}{n}\sum_{i=1}^{n} f^*_{FBG}(\mathbf{\Lambda}) = \min_{\mathbf{\Lambda}} \frac{1}{n}\sum_{i=1}^{n}\left(\frac{1}{\sigma_i^2(1+\gamma\cos(\psi_i))}(\| \overrightarrow{c_1x_i}\| + \|\overrightarrow{c_2x_i}\| - 2a)^2\right). \tag{6}$$

When solving the minimisation problem, an iterative parameter update, determined by the gradient of the error function $f^*_{FBG}(\mathbf{\Lambda})$, assists in making the least-squares algorithm stable and convergent. The gradients of the objective function in Eq. (6), with respect to the five ellipse parameters $\mathbf{\Lambda}$, are derived in Appendix B. The new FBG objective function is minimised iteratively to solve for the five parameters in $\mathbf{\Lambda}$ using the gradients to determine gradient descent direction.

A similar revision to Eq. (3) is carried out to obtain a heteroscedastic objective function for the ODG model, where f_{ODG} is replaced by $f^*_{ODG}(\mathbf{\Omega}) = \frac{1}{\sigma_i^2}f_{ODG}(\mathbf{\Omega})$. Using the direct, FBG and ODG fitting models of the edge points, the identified image features are characterised by precise sub-pixel locations and dimensions even in the presence of noise. The performances of the new heteroscedastic FBG and ODG ellipse models are investigated in Section 3.

2.5. Metric sphere measurements

After the spherical features are detected and fully characterised as ellipses in images, the metric positions and sizes of the spheres need to be evaluated. This evaluation requires knowledge of the intrinsic and extrinsic parameters of the two or more cameras needed to map the 3D world position of the spheres to the respective 2D images of the cameras. Throughout Section 3.5, the parameters of the three vision cameras used in this paper are assumed to be predetermined. The details on how the camera parameters are characterised can be found elsewhere [55,64,65].

2.5.1. Image projection mapping

The intrinsic parameters of a camera facilitate the mapping of the projection of 3D world points onto the camera's 2D image plane, where the 3D points are expressed in the camera coordinate system (CCS) located at the camera centre. As illustrated in Fig. 5, the camera A maps the camera-centric 3D point $X_A = [x_A, y_A, z_A]^\top$ to the corresponding 2D image point $x_A = [u_A,\ v_A]^\top$ through the linear expression $\begin{bmatrix} x_A \\ 1 \end{bmatrix} = \frac{1}{z_A}K_AX_A$, where K_A is the camera calibration matrix given by

$$K_A = \begin{bmatrix} f_u & 0 & c_u \\ 0 & f_v & c_v \\ 0 & 0 & 1 \end{bmatrix}_A. \tag{7}$$

The principal point coordinates $x_c = [c_u, c_v]^\top$ and the pixel-scaled focal lengths $[f_u, f_v]^\top$ of the camera form the calibration matrix of Eq. (7). A 3D point $X_W = [x_W, y_W, z_W]^\top$, expressed in an arbitrary world coordinate system (WCS), needs to be transformed to the CCS before going through the projection mapping. The camera parameters that describe the transformation from a WCS to a CCS are called the extrinsic

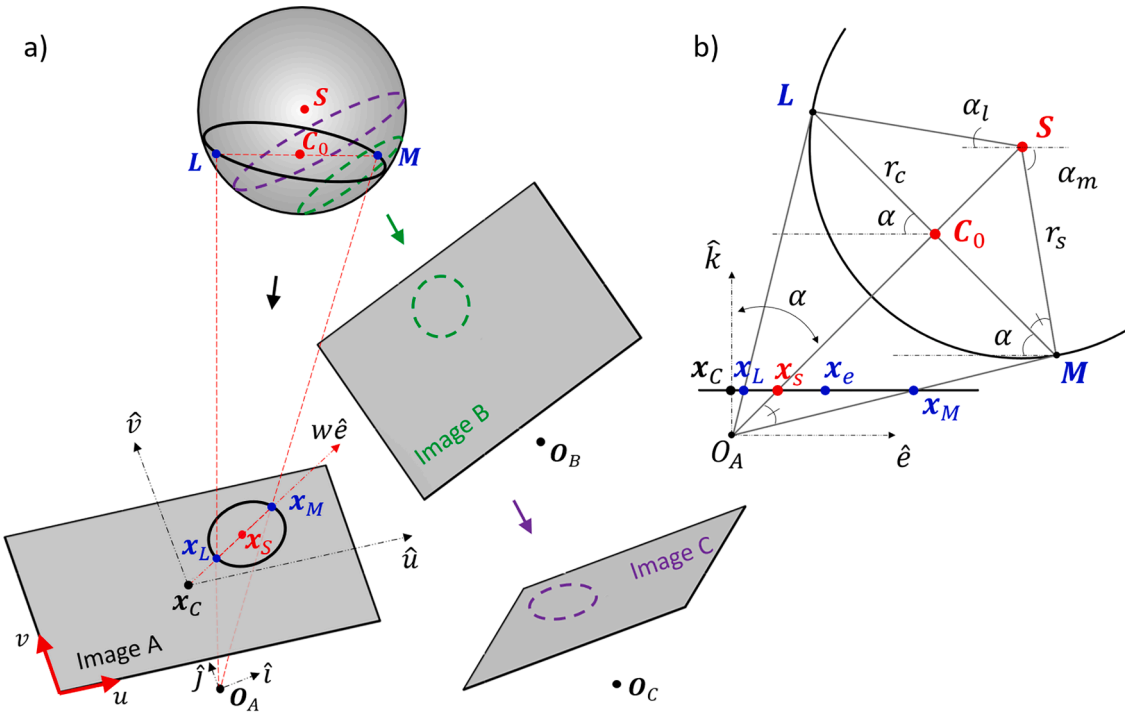

Fig. 6. Ellipse features in three cameras A, B and C where each camera observes projection of different tangential circles on the sphere in a). The geometric sketch of plane containing the major axis ($\overrightarrow{x_L x_M}$) on image A and 3D points $\boldsymbol{L}$ and $\boldsymbol{M}$ on a tangential circle in a) is given in b).

parameters. Assigning $\boldsymbol{T}_W^A$ as the transformation matrix from WCS to CCS, the general projection mapping of a vision camera can be expressed as

$$\begin{bmatrix} \boldsymbol{x}_A \\ 1 \end{bmatrix} = \omega_A \boldsymbol{K}_A \boldsymbol{T}_W^A \begin{bmatrix} \boldsymbol{X}_W \\ 1 \end{bmatrix}, \tag{8}$$

where $\omega_A = \frac{1}{z_A}$ for $[x_A, y_A, z_A]^\top = \boldsymbol{T}_W^A \begin{bmatrix} \boldsymbol{X}_W \\ 1 \end{bmatrix}$.

In practice, the linear mapping between $\boldsymbol{X}_W$ and $\boldsymbol{x}_A$ only holds after correction of lens distortion—the dominant distortion type is the radial distortion [18,66]. Since Brown [67] proposed the radial polynomial distortion model, it has become the conventional radial distortion model, giving rise to various methods of carrying out inverse radial distortion solutions [68]. Assuming the raw pixel coordinates captured from the camera are $[\widetilde{u}, \widetilde{v}]^\top$, the distortion-corrected pixels $[u, v]^\top$ are expressed in terms of the radial distortion coefficients $\{k_1, k_2, k_3, \ldots k_n\}$ and the distortion centre $[d_u, d_v]^\top$ in

$$\begin{bmatrix} \widetilde{u} \\ \widetilde{v} \end{bmatrix} = \left(1 + \sum_{i=1}^{n} k_i \left((u - d_u)^2 + (v - d_v)^2 \right)^i \right) \begin{bmatrix} u \\ v \end{bmatrix}. \tag{9}$$

For the vision system in this paper, tangential distortion was found to be negligible and is, therefore, not considered.

When an artefact, such as checkerboard is imaged, the known physical dimensions of the artefact and the observed distorted dimension of the artefact can be used to solve for the inverse of the distortion model in Eq. (9). The raw pixel data $[\widetilde{u}, \widetilde{v}]^\top$, obtained by imaging a checkboard artefact during the camera pre-calibration process, is used to solve the inverse distortion problem by determining the radial distortion coefficients and the distortion centre. amongst the methods for solving the inverse radial distortion problem, iterative methods are reported to give the best results [68]. The distortion model in Eq. (9) is normally truncated to a finite value of n, where higher values of n are used for more demanding applications. It is often the case that the distortion centre is taken as the principal point of the camera—MATLAB and OpenCV vision algorithms commonly make this simplification. Therefore, the MATLAB stereo camera characterisation implemented in this paper uses the simplification $[d_u, d_v]^\top = \boldsymbol{x}_c$ and the maximum number of radial distortion coefficients supported by the MATLAB application ($n = 3$). However, the trinocular camera characterisation algorithm developed for this paper uses an independent value for the radial distortion centre and a higher number of radial distortion coefficients $n = 6$ [55]. It should be noted that the computations for lens distortion correction are carried out during the pre-calibration process, when the camera intrinsic and extrinsic parameters are evaluated, after which corrected pixels $\boldsymbol{x}_A = [u, v]^\top$ can be used in Eq. (8).

From an ellipse feature detected from a camera, we do not have enough information to evaluate the sphere 3D coordinate and diameter. One or more additional cameras are required for 3D measurement of the sphere. Fig. 6a) shows the boundaries of the ellipse features imaged by three cameras as a result of the projections of the corresponding spherical tangential circles. Each observation of the sphere from the three views is a result of projection of a different tangential circle on the sphere. Therefore, reconstruction of the size and location of the sphere from its image projections requires evaluation of the relationship between the multi-view ellipse features.

2.5.2. *Ellipse eccentricity error*

When a sphere is viewed from an angle away from the principal axis of a camera, the projection of the centre of the sphere does not exactly match the centre of the observed ellipse feature. The actual projection of the sphere centre is not available from the acquired image of the sphere and must be derived from the observable ellipse feature in the image. The Euclidean distance, shown in Fig. 6b), between the ellipse centre $\boldsymbol{x}_e$ and the actual projection of the sphere centre $\boldsymbol{x}_s$ is referred to as the eccentricity error [69].

Given that the projection of a sphere centre is located along the radial line joining the principal point and the ellipse centre [29,36], we investigate the sphere points $\boldsymbol{L}$ and $\boldsymbol{M}$ whose projections also lay along the radial direction (see Fig. 6). The radial line coincides with the ellipse major axis; therefore, the values of $\boldsymbol{x}_L$ and $\boldsymbol{x}_M$ (the projection of the 3D points $\boldsymbol{L}$ and $\boldsymbol{M}$ respectively) are known from the detected ellipse

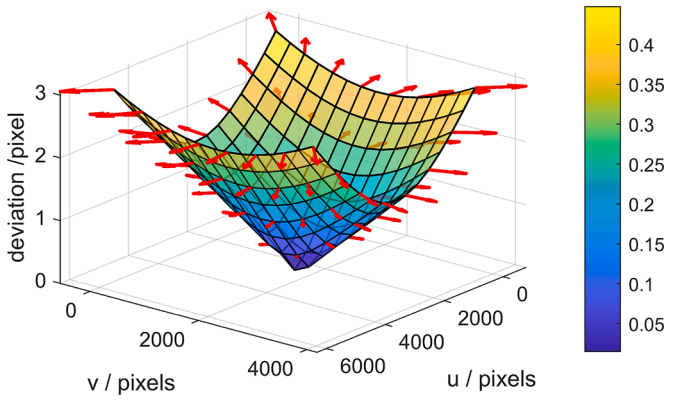

Fig. 7. Eccentricity error $\boldsymbol{x}_e - \boldsymbol{x}_s$ is plotted for pixel positions at camera depth of $z_A = 500$ mm for a 30 mm diameter sphere. The colour map shows the ellipse eccentricity and arrows indicate the direction of the eccentricity error.

features from Section 2.4. Fig. 6b) isolates the plane of light containing $\boldsymbol{L}$,$\boldsymbol{M}$ and the radial line on the image, where the ellipse centre $\boldsymbol{x}_e$ divides the distance between $\boldsymbol{x}_L$ and $\boldsymbol{x}_M$ equally by the ellipse semi-major axis a. The angle α, in Fig. 6b), can be evaluated from

$$\alpha = \frac{1}{2}\tan^{-1}\left(\frac{\| \boldsymbol{x}_e - \boldsymbol{x}_c\| - a}{f_{uv}}\right) + \frac{1}{2}\tan^{-1}\left(\frac{\| \boldsymbol{x}_e - \boldsymbol{x}_c\| + a}{f_{uv}}\right) \tag{10}$$

where f_{uv} is the equivalent focal length in pixels along the unit radial direction $\widehat{\boldsymbol{e}}$. The value of f_{uv} can be derived from the known pixel-scaled focal lengths $[f_u, f_v]^\top$, the principal point $\boldsymbol{x}_c = [c_u, c_v]^\top$ and the ellipse centre $\boldsymbol{x}_e = [u_e, v_e]^\top$ as

$$f_{uv} = \sqrt{\frac{(u_e - c_u)^2 f_u^2 f_v^2 + (v_e - c_v)^2 f_u^2 f_v^2}{(u_e - c_u)^2 f_v^2 + (v_e - c_v)^2 f_u^2}}. \tag{11}$$

The sphere centre image location is then obtained as $\boldsymbol{x}_s = f_{uv}\tan(\alpha)\widehat{\boldsymbol{e}}$ and the eccentricity error vector can be expressed as $\Delta\boldsymbol{w} = \boldsymbol{x}_e - f_{uv}\tan(\alpha)\widehat{\boldsymbol{e}}$ using Eq. (10) and Eq. (11) to evaluate α.

To demonstrate the value of the eccentricity error in our vision system, the error is evaluated at arbitrary 3D sphere positions. For a sphere with diameter of 30 mm placed at the camera depth of $z_A = 500$ mm, the eccentricity error vector $\boldsymbol{x}_e - \boldsymbol{x}_s$ across the camera image plane is shown in Fig. 7. For the $[u, v]^\top$ pixel positions on the image, the vertical axis and the colour map in Fig. 7 show the eccentricity error and the ellipse eccentricity respectively. The direction of the eccentricity error vector is indicted by the arrows that have lengths proportional to the magnitude of the eccentricity error. It is observed that the eccentricity error increases as the sphere is viewed from a farther angle from the principal axis of the camera and the error vector is directed radially from the principal point $\boldsymbol{x}_c$ on the image plane.

2.5.3. Image feature correspondence

To be able to reconstruct the 3D positions of spheres from their multi-camera images, it is necessary to determine the correspondence between the multi-view features detected in the images. Corresponding image features resulting from projections of a 3D object in multiple cameras are related by multi-view geometric relationships [65], that enable reconstruction of the 3D coordinates of the object. Therefore, from sets of features detected from different views, we investigate the criteria for evaluating image feature correspondences.

For a binocular case, the epipolar constraint that defines the relationship between two corresponding image points $\boldsymbol{x}_A$ and $\boldsymbol{x}_B$, from camera A and B respectively, is expressed as

$$\delta_{AB}(\boldsymbol{x}_A, \boldsymbol{x}_B) = \omega_l \begin{bmatrix} \boldsymbol{x}_B \\ 1 \end{bmatrix}^\top \boldsymbol{F}_{AB} \begin{bmatrix} \boldsymbol{x}_A \\ 1 \end{bmatrix}, \tag{12}$$

where $\delta_{AB} \approx 0$, $\boldsymbol{F}_{AB}$ is the fundamental matrix of binocular camera pair AB and ω_l is the Euclidean normalisation factor of the epipolar line $\boldsymbol{F}_{AB}\begin{bmatrix} \boldsymbol{x}_A \\ 1 \end{bmatrix}$. An image feature $\boldsymbol{x}_A$ from camera A corresponds to another image feature $\boldsymbol{x}_B$ from camera B if $\delta_{AB}(\boldsymbol{x}_A, \boldsymbol{x}_B)$ satisfies $\| \delta_{AB}(\boldsymbol{x}_A, \boldsymbol{x}_B) \| < \delta_{max}$ and $\boldsymbol{x}_B$ results in the minimum value of $\| \delta_{AB}(\boldsymbol{x}_A, \boldsymbol{x}_B) \|$ for all candidate features observed from camera B. The value of the pixel threshold δ_{max} is chosen between 0.5 to 3 pixels. Epipolar constraints similar to Eq. (12) can be expressed for the other camera pairs AC and BC using their respective fundamental matrices $\boldsymbol{F}_{AC}$ and $\boldsymbol{F}_{BC}$. The fundamental matrices $\boldsymbol{F}_{AB}$, $\boldsymbol{F}_{AC}$ and $\boldsymbol{F}_{BC}$ represent the geometric relationships between the corresponding camera pairs and are predetermined during camera characterisation.

The binocular correspondence criteria can effectively find corresponding features and erroneous correspondences are scarce. In theory, the binocular criteria can be prone to correspondence errors that can be resolved by considering an additional third camera. A three-camera system can be simply modelled as a multi-binocular system with multiple fundamental matrices or a trinocular system where the internal relationship in the three-view system is encapsulated in a single trifocal tensor. Compared to the multi-binocular vision system, the trifocal tensor of the trinocular vision system provides better three-view agreement and a more compact model. In Einstein notation, three image points $\boldsymbol{x}_A$, $\boldsymbol{x}_B$ and $\boldsymbol{x}_C$ observed from cameras A, B and C respectively correspond to one another if $\boldsymbol{\delta} \approx 0_{3\times 3}$ in

$$\delta_{st} = x_A^i x_B^j x_C^k \epsilon_{jqs} \epsilon_{krt} T_i^{qr}, \tag{13}$$

where T_i^{qr} is the trifocal tensor, ϵ_{ijk} represents the Levi-Civita tensor and $\{i, j, k, q, r, s, t\}$ are the indices of the Einstein notation. Hence, similar to the binocular criteria, correspondence amongst candidate image feature triplets can be determined using Eq. (13).

2.5.4. Sphere 3D position and size

The 3D coordinates of sphere centres are evaluated by triangulation of the corresponding image locations from two or more views. Considering cameras A and B, sphere centre projections $\boldsymbol{x}_A$ and $\boldsymbol{x}_B$ (from cameras A and B respectively) are triangulated to determine the 3D coordinates of the sphere centre $\boldsymbol{S}$. The MATLAB computer vision toolbox is used to carry out the binocular triangulation to determine $\boldsymbol{S}$. For the trinocular system of cameras A, B and C, a triangulation solver is developed using least squares to determine $\boldsymbol{S}$. Using Eq. (8) and assigning $\boldsymbol{S}$ in the CCS of camera A (at $\boldsymbol{O}_A$ in Fig. 6), the projection mapping of the point $\boldsymbol{S}$ in the three cameras can be expressed as: $\begin{bmatrix} \boldsymbol{x}_A \\ 1 \end{bmatrix} = \omega_A \boldsymbol{K}_A \boldsymbol{S}$, $\begin{bmatrix} \boldsymbol{x}_B \\ 1 \end{bmatrix} = \omega_B \boldsymbol{K}_B \boldsymbol{T}_A^B \begin{bmatrix} \boldsymbol{S} \\ 1 \end{bmatrix}$ and $\begin{bmatrix} \boldsymbol{x}_C \\ 1 \end{bmatrix} = \omega_C \boldsymbol{K}_C \boldsymbol{T}_A^C \begin{bmatrix} \boldsymbol{S} \\ 1 \end{bmatrix}$. After restructuring terms in the three projection equations, the unknown $\boldsymbol{S}$ is evaluated using a least-squares solution based on singular value decomposition (SVD) [65]. It should be noted that the values of the camera matrices $\boldsymbol{K}_A$, $\boldsymbol{K}_B$ and $\boldsymbol{K}_C$, and the transformation matrices $\boldsymbol{T}_A^B$ and $\boldsymbol{T}_A^C$ are part of the predetermined camera parameters.

The size of the sphere can also be evaluated from the elliptical features determined in the images. Referring to Fig. 6b), the radius of the sphere is related to the size of the image ellipse by

$$2a = f_{uv}\left(\frac{\sqrt{x_s^2 + y_s^2} + r_s\cos(\alpha_m)}{z_s - r_s\sin(\alpha_m)} - \frac{\sqrt{x_s^2 + y_s^2} - r_s\cos(\alpha_l)}{z_s + r_s\sin(\alpha_l)}\right), \tag{14}$$

where $\boldsymbol{S} = [x_s, y_s, z_s]^\top$, $\alpha_m = \tan^{-1}\left(\frac{\|\boldsymbol{x}_e - \boldsymbol{x}_c\| + a}{f_{uv}}\right)$ and $\alpha_l = \tan^{-1}\left(\frac{\|\boldsymbol{x}_e - \boldsymbol{x}_c\| - a}{f_{uv}}\right)$. We can simplify Eq. (14) into a simple quadratic equation in the form $\zeta_1 r_s^2 + \zeta_2 r_s + \zeta_3 = 0$ and find r_s as

Algorithm 1
Identification of measured spheres using calibrated artefact data.

Input: connectivity ($\mathscr{G}_a$, $\mathscr{C}_a$) and dimension data ($\mathscr{E}_a$, $\mathscr{S}_a$) of artefact, measured coordinate and size data ($\mathscr{X}_m$, $\mathscr{S}_m$)
Output: correspondence between measured spheres and calibrated artefact data (n_m, n_a)
$\mathscr{G}_m \leftarrow$ construct undirected graph from ($\mathscr{X}_m$, $\mathscr{S}_m$) for distances and sizes matching ($\mathscr{E}_a$, $\mathscr{S}_a$)
$\mathscr{C}_m \leftarrow$ find all tricycles in graph $\mathscr{G}_m$ where nodes are numbered $k = 1,2,\ldots k_n$
($\mathscr{C}^t_m$, $\mathscr{C}^t_a$)$\leftarrow$ tokenize tricycles from node triplets in $\mathscr{C}_m$ and $\mathscr{C}_a$ to searchable string tokens
($\boldsymbol{n}_m$, $\boldsymbol{n}_a$)$\leftarrow$ initialize arrays $\boldsymbol{n}_m$ and $\boldsymbol{n}_a$ with size equal to k_n (number of nodes in $\mathscr{G}_m$)
$\boldsymbol{M}\leftarrow$ initialize a 2D list with k_n rows
for every tricycle token $t_i (i = 1,2\ldots i_n)$ in $\mathscr{C}^t_m$:
  $t_a \leftarrow$ search for the token in $\mathscr{C}^t_a$ that contains identical characters in t_i
  (c^*_m, c_a)$\leftarrow$ find the tricycle nodes corresponding to t_i in $\mathscr{C}_m$ and t_a in $\mathscr{C}_a$
(c^*_m, t_i)$\leftarrow$ adjust order of nodes in c^*_m(and token t_i) to CCW direction if it is CW
  ($t^{'}_i, t^{''}_i$)$\leftarrow$ find variations of t_i: $t^{'}_i = [t_i(3:6), t_i(1:2)]$ and $t^{''}_i = [t_i(5:6), t_i(1:4)]$
  if t_i matches t_a:
    $c_m \leftarrow c^*_m$
  elseif $t^{'}_i$ matches t_a:
    $c_m \leftarrow [c^*_m(2:3), c^*_m(1)]$ move the first node to the end
  elseif $t^{''}_i$ matches t_a:
    $c_m \leftarrow [c^*_m(3), c^*_m(1:2)]$ move the third node to the beginning
  end
  for $j = 1,2\ldots 3$
    $\boldsymbol{n}_m(c_m(j)) \leftarrow c_m(j)$
    $\boldsymbol{M}(c_m(j)) \leftarrow$ add the artefact matching node $c_a(j)$ to row number $c_m(j)$ of $\boldsymbol{M}$
  end
end
$\boldsymbol{n}_a \leftarrow$ find the mode of node entries in each row in $\boldsymbol{M}$

$$r_s = -\frac{\zeta_2}{2\zeta_1} - \frac{\sqrt{\zeta_2^2 - 4\zeta_1\zeta_3}}{2\zeta_1}, \tag{15}$$

where the quadratic terms are defined as:

$$\zeta_1 = \sin(\alpha_m - \alpha_l) - \frac{2a}{f_{uv}}\sin(\alpha_m)\sin(\alpha_l)$$

$$\zeta_2 = \frac{2a}{f_{uv}} z_s(\sin(\alpha_l) - sin(\alpha_m)) - (\sin(\alpha_l) + \sin(\alpha_m))\sqrt{x_s^2 + y_s^2} - z_s(\cos(\alpha_m) + \cos(\alpha_l))$$

$$\zeta_3 = \frac{2a}{f_{uv}} z_s^2.$$

The 3D position and size of all detected spheres can be accurately calculated using the triangulation solver for $\boldsymbol{S}$ and Eq. (15) respectively. Further refinement of the sphere 3D coordinates is possible using iterative minimisation of the geometric objective functions, where the SVD-based solution is used as an initial guess for the iteration [65].

2.5.5. Sphere identification

A final sphere identification process is suggested to match the measured spheres with the calibrated artefact data. The identification process provides a means of both labelling and checking the spatial consistency of the measured sphere features. When the artefact position is changed, sphere identification makes it possible to reliably track changes in sphere positions and relate them to the traceable artefact calibration data.

The identification of spheres relies on the spatial encoding of the size and distance dimensions of the measurement artefact. The deliberate combination of sphere connectivity, sphere sizes $\mathscr{S}_a$ and spacings $\mathscr{E}_a$, in Tables 1 and 2 respectively, ensures that the identification of adjacent sphere triplets is possible. We organise the calibrated artefact and measured sphere information into undirected graphs for easy implementation of the identification algorithm using graph theory [70]. Algorithm 1 summarises the identification process for a set of sphere coordinates $\mathscr{X}_m$ and sphere sizes $\mathscr{S}_m$ measured from corresponding binocular or trinocular images.

The calibrated dimensions of the manufactured target in Tables 1 and 2 are organised into a graph $\mathscr{G}_a$, such that the indices of the spheres are the nodes where adjacent spheres share an edge. Bearing no sphere, Node 1 was reserved as the attachment point of the artefact to the motion systems and, therefore, is not linked to the other nodes. The identification method determines the nodes of a subgraph $\mathscr{G}_m$ formed by some measured spheres by comparing all adjacent node triples (referred to as tricycles) in the subgraph to the nodes in the main graph $\mathscr{G}_a$. $\mathscr{C}_a$ is the set of all tricycles in $\mathscr{G}_a$ and is an input to Algorithm 1 where the nodes and edges in the measured tricycle set $\mathscr{C}_m$ are searched for. For every matching tricycle, the index of nodes in $\mathscr{G}_a$ matching nodes in $\mathscr{G}_m$ are recorded in $\boldsymbol{M}$. For all the tests carried out in this paper, there has not been any contradiction in matched nodes between $\mathscr{G}_a$ and $\mathscr{G}_m$. Algorithm 1 outputs the arrays $\boldsymbol{n}_m$ and $\boldsymbol{n}_a$ which are the corresponding indices of nodes in graphs $\mathscr{G}_m$ and $\mathscr{G}_a$ respectively. Fig. 8 shows a subgraph of six measured sphere nodes after they have been matched

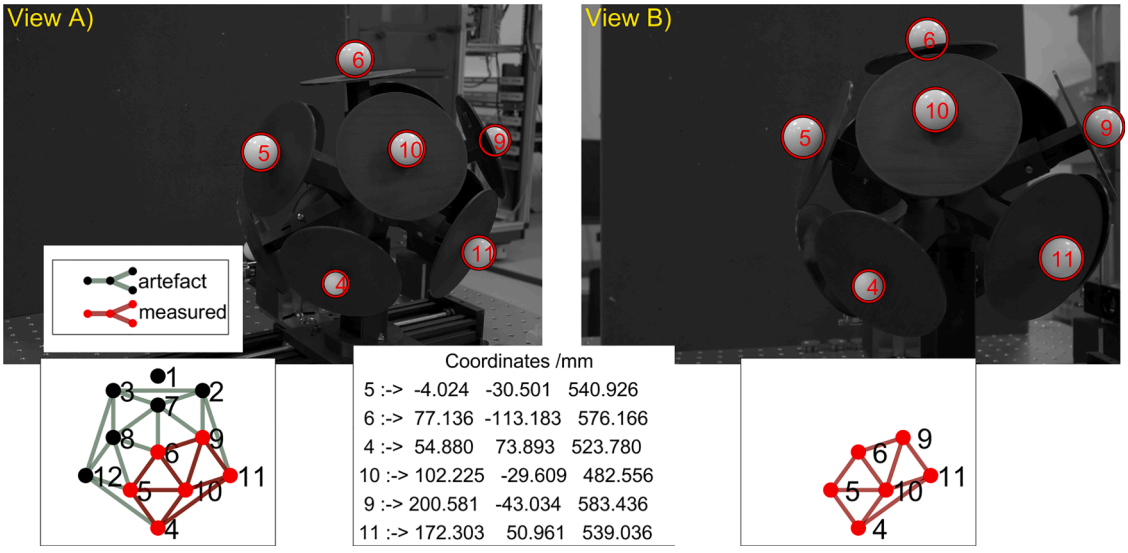

Fig. 8. Identification of measured spheres using sphere graph data of the calibrated artefact and the measured spheres. The corresponding sphere indices {4, 5, 6, 9, 10, 11} from the calibrated artefact data are shown in views A and B, which are obtained from cameras A and B respectively. The identified subgraph $\mathscr{G}_m$ of the measured spheres using Algorithm 1 is overlaid on the overall artefact graph $\mathscr{G}_a$. The 3D coordinates of the centres of the measured spheres are also given.

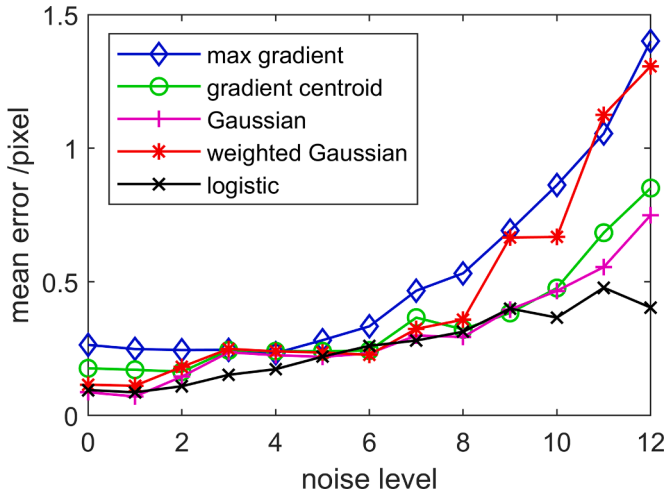

Fig. 9. Error of edge localisation methods evaluated as the mean of orthogonal deviations of edge points evaluated at different image noise and degradation levels.

with the full artefact graph. The identification graphs at displaced positions of the artefact can be found in the supplementary GIF video submitted with this paper (see the supplementary material section).

3. Performance assessment

The performance of the methods used for feature localisation and sphere measurement are compared using some verification tests in this section. First, the robustness and computational complexity of the investigated edge and ellipse localisation methods are evaluated. Next, the measurement quality of the measured sphere coordinates and sizes is analysed. Lastly, the errors in the displaced sphere positions are investigated through an interferometry displacement experiment.

3.1. Robustness and computational complexity

Due to the presence of noise in electronic systems, it is critical to evaluate how image-based algorithms are able to operate in the presence of noise. Robustness analysis of image algorithms provides the necessary performance metric to assess whether an algorithm can be considered robust given a tolerance for the level of noise and image degradation [71]. The robustness of the edge and feature localisation methods, discussed in Sections 2.3 and 2.4 respectively, provides vital information about the algorithmic performance of the methods in the presence of noise. Using robustness measures, we can compare how different localisation and edge models perform at various noise levels. Since robustness analysis in MV depends on knowing the level of degradation and the accurate scale of the noise, determining robustness using the actual experimental images that already contain unknown noise from various sources can be challenging.

A common approach for robustness assessment involves the use of synthetic images, where the addition of varying levels of noise can be used for the assessment [72,73]. By adding perturbations, such as additive, multiplicative and speckle noise to synthetic images using the script in reference [74], we investigated the error in the edge points sampled using different edge localisation methods in the presence of varying image degradation levels. Fig. 9 shows the mean error of the evaluated edge points from 100 generated samples of synthetic images using five edge localisation methods—the maximum gradient, gradient-weighted centroid, Gaussian, weighted Gaussian and logistic methods. Details on these edge localisation methods are discussed in Section 2.3. Overall, the logistic and Gaussian edge spread models are more robust when compared with the other methods. The weighted Gaussian method results in errors that are between the errors observed in the maximum gradient and the Gaussian edge points. As a result of the gradient cut-off points introduced to reduce the noise-sensitivity of the Gaussian fitting presented in Section 2.3, the Gaussian edge points perform more robustly than the weighted-Gaussian edge points.

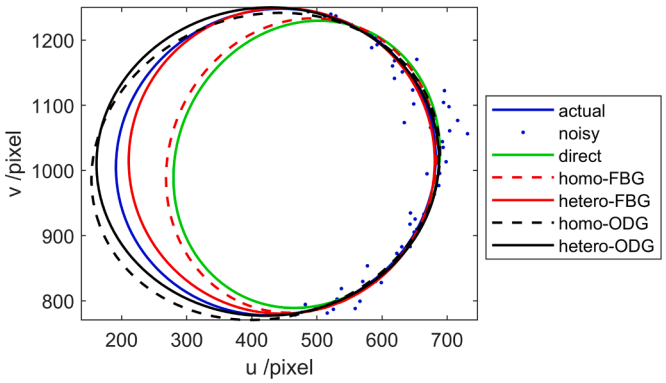

Fig. 10. An ellipse (in colour blue) is partially sampled and degraded by noise to illustrate the robustness of the direct, homoscedastic FBG (homo-FBG), heteroscedastic FBG (hetero-FBG), homoscedastic ODG (homo-ODG) and heteroscedastic (hetero-ODG) ellipse fitting models.

When actual images (accessible from the reference [75]) are used, the logistic fitting method is observed to be highly sensitive to variations in brightness and shadows around the sphere edges. The reason why the logistic fitting method is more sensitive is that large portions of edge profiles are required for the convergence of the iterative logistic solver. The wideness of the edge profile used for fitting the logistic function makes the solver susceptible to noise (at low SNR), background variations and shadows. As a result, the logistic method does not outperform the Gaussian and centroidal edge localisation methods on actual images.

In addition to the use of a robust edge localisation method, the ellipse fitting model should also be robust to noise. By adding orthogonal and normally-distributed noise to the sampled ellipse edge points shown in Fig. 10, we fit ellipses using the models discussed in Section 2.4. The edge points are sampled from only the right side of the ellipse to accentuate the variations in the shapes of the fitted ellipses. The random orthogonal deviations $\mathcal{N}(0, \boldsymbol{\sigma}_n^2)$ are sampled from normal PDFs with varying standard deviations $\boldsymbol{\sigma}_n$ and zero means. The variance of the added noise is chosen such that $\boldsymbol{\sigma}_n$ has values between zero and thirty pixels. Based on the fitted ellipses shown in Fig. 10, the direct [31] and homoscedastic FBG [32] models are far from the original ellipse. The proposed models in this paper—the heteroscedastic FBG and ODG models—improve the fitting of the respective homoscedastic FBG and ODG models.

To quantitatively compare the results from the data shown in Fig. 10, using the normalised ellipse error defined in reference [32], 1000 randomly generated ellipses are investigated with varying ellipse shapes and noise levels. The normalised ellipse error is the normalised area of the exclusive disjunction (XOR operation $\oplus$) of a fitted ellipse $\boldsymbol{\Omega}$ and the actual ellipse $\boldsymbol{\Omega}_0$ given by

$\frac{\mathscr{A}(\boldsymbol{\Omega} \oplus \boldsymbol{\Omega}_0)}{\mathscr{A}(\boldsymbol{\Omega}_0)}$, where $\mathscr{A}$ is the area function of a closed 2D pixel region.

From Fig. 11a), the direct algebraic ellipse fitting model results in the highest increase in ellipse error as the noise level is increased. The homoscedastic FBG model in Fig. 11b) shows little improvement over the direct model, while the heteroscedastic FBG model reduces the normalised error by more than a factor of three for very noisy data. A significant improvement is also observed in Fig. 11c) when the heteroscedastic ODG model is compared to its homoscedastic counterpart.

From the results in this section, it is shown that the methods used for edge localisation and ellipse fitting affect how robustly sphere features are detected. It is important to investigate the computational cost that

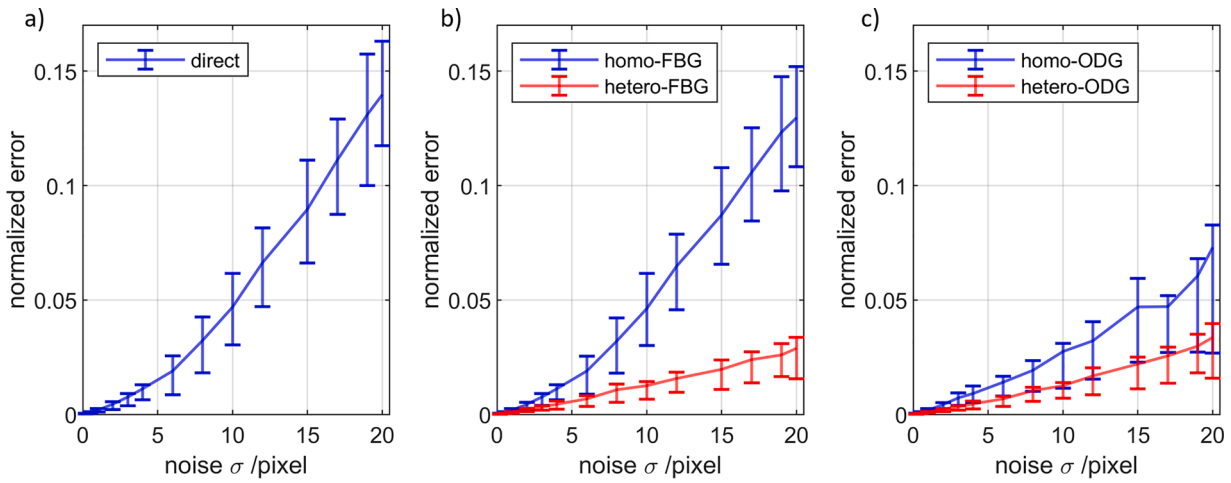

Fig. 11. Error comparison of fitted ellipses at increasing noise levels. Plot lines show the mean normalized error and error bars show the minimum and maximum error observed for 1000 ellipses.

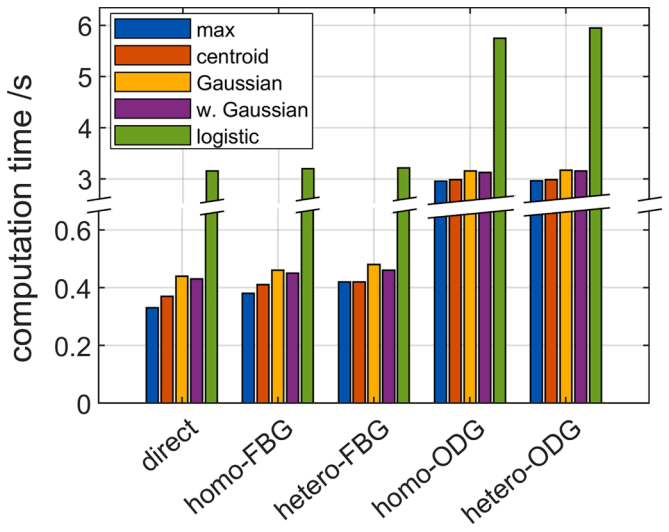

Fig. 12. Average image computation time for different combinations of edge localisation and ellipse fitting algorithms.

comes along with using more robust methods. On a computer running on Windows 11 operating system, equipped with an Intel i7–11800H eight-core processor and 16 Gb RAM, the average time elapsed, per image, to detect the spheres are shown in Fig. 12. amongst the edge localisation methods, the iterative logistic edge spread solution has the highest order of computational complexity, taking around ten times the computation time of the other edge localisation methods. Similarly, the ODG model, requiring two-stage iteration, exhibits high computational time as a result. Considering both robustness and computational complexity, the Gaussian and centroid edge localisation methods in conjunction with the heteroscedastic FBG ellipse model show favourable performance. The heteroscedastic FBG ellipse model provides high robustness to noise, similar to the ODG model, but with a much faster computation time.

Based on the findings presented in this section, we deduce that the gradient-centroid-based edge localization method offers a more computationally less expensive alternative to the Gaussian-based localisation method, although it may exhibit slightly lower robustness. The proposed heteroscedastic FBG and ODG ellipse models significantly improve robustness of the geometric fitting models. When the heteroscedastic FBG model is implemented with the centroidal or Gaussian localisation method, robustness performance similar to the heteroscedastic ODG model is achieved with computation time reduced by up to a factor of ten.

3.2. *Measurement quality*

Relying on the calibrated artefact measurements shown in Table 1 and Table 2, the quality of the measured coordinate positions of the vision system are evaluated. A multi-sphere artefact is suitable for use as a verification test artefact in the ISO and VDI/VDE standard documents on optical CMSs [24,25]. The performance of the vision-based CMS in this paper is assessed using quality parameters that are evaluated and reported in accordance with the VDI/VDE 2634 definitions [25]. By assessing the quality parameters, we can gain a comprehensive understanding of the performance of the image localisation algorithm options

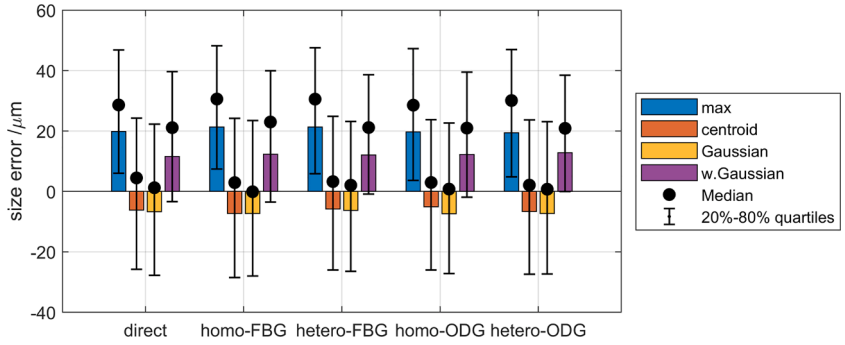

Fig. 13. Size error distributions for various edge localisation methods and ellipse fitting models. The bars indicate the mean error, and the error bars show the 20 % and 80 % lower and upper quartiles of the error distributions respectively.

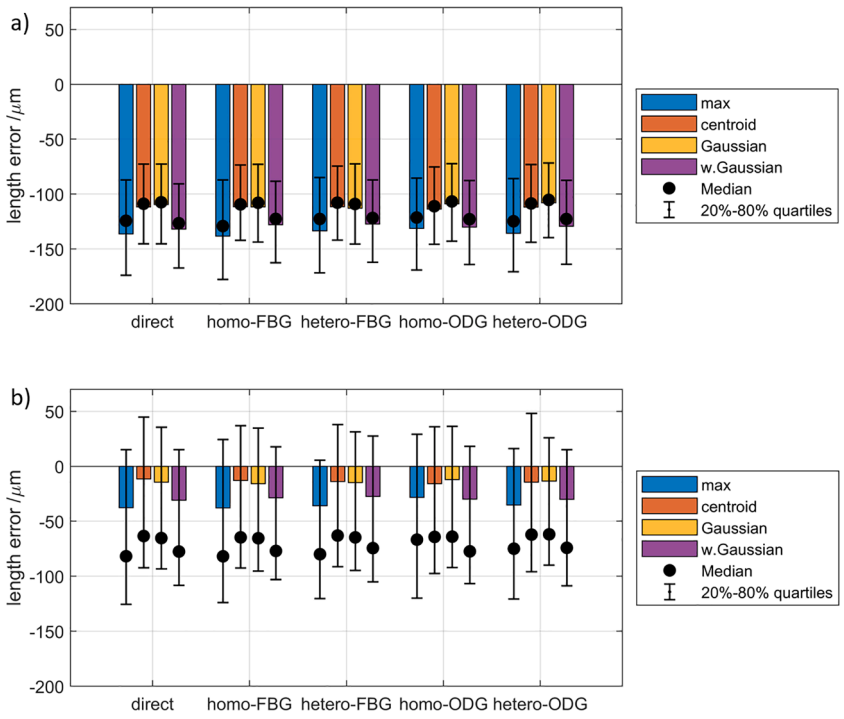

Fig. 14. Length measurement errors of edge localisation methods and ellipse feature models for a) the binocular CMSs and b) the trinocular CMS. The bars indicate the mean error and the error bars show the 20 % and 80 % lower and upper quartiles of the error distributions respectively.

presented in this paper.

Evaluated sphere sizes calculated from Eq. (15) are verified using the probing size error quality parameter, which is defined as the difference between a measured sphere diameter and the calibrated diameter of the same sphere [25]. Fig. 13 shows the size error distribution (within the 20th and 80th quartile) of the artefact spheres for the different image edge localisation methods discussed in this paper. The size errors are evaluated at eleven evenly spaced positions along the travel range of the linear actuator from the experimental setup shown in Fig. 2. For each of the edge localisation methods, the size error distributions consist of errors evaluated from five repeated experiments using AB, AC and BC binocular camera pairs. From Fig. 13, the feature edges defined by the maximum gradient pixel positions consistently overestimate the sphere sizes and result in the highest systematic size errors. The weighted Gaussian edge localisation method moves Gaussian localisation edges closer to the maximum gradient pixel positions, which increases the systematic size error in this application. The gradient centroid and Gaussian edge locations exhibit the least systematic errors, with majority of the size errors falling below 20 μm.

Probing size error qualifies the error behaviour of the measurement system in localised regions where the images of the spheres are captured. To assess measurement quality spanning multiple localised regions, another important quality parameter, known as length measurement error, should be evaluated. Specifically, the length measurement error is defined as the difference between the sphere spacings measured by an optical CMS and the calibrated spacings between the spheres, as detailed in standard documents [24,25]. The measured sphere coordinate positions presented in Section 2.5 are validated using the error in the distances between every pair of detected spheres, as gauged from the calibrated artefact sphere spacings. The measured distances between the spheres range from approximately 107 mm to 210 mm, depending on the spacings between all sphere pairs detected in each image.

Fig. 14 shows the comparison of the length measurement error of the binocular and trinocular CMSs for the different edge location and ellipse feature models given in Sections 2.3 and 2.4 respectively. The length errors are evaluated using the same set of images used for the size measurement verification. Fig. 14a) shows length errors for binocular camera pairs and Fig. 14b) shows the same errors for coordinate positions measured from the trinocular CMS. The bars in Fig. 14 indicate the mean of the length errors and the error bars show the distribution using a 20 % lower quartile, median and 80 % upper quartile.

Both Fig. 14a) and Fig. 14b) show that the length measurements are predominantly underestimated, and the type of ellipse feature model employed does not have a noticeable influence on the length errors. This is most likely due to the low levels of noise and degradation in the images—the same applies to the probing size error results in Fig. 13. Evidently, even for a partially sampled ellipse (such as the ellipse in Fig. 10), the difference in the performance of the ellipse models becomes less apparent as the noise level diminishes, as shown in Fig. 11.

For the edge localisation methods, the method used for extracting edge points significantly affects the length measurement error. In agreement with the probing size errors, the gradient centroid and Gaussian edge localisation techniques tend to yield lower mean length errors compared to the other methods shown in Fig. 14. Specifically, the maximum gradient edge localisation method tends to have the highest mean length error, while slightly lower errors are observed with weighted Gaussian edge points.

The trinocular measurements shown in Fig. 14b) demonstrate a reduced systematic length error in comparison to the binocular measurements shown in Fig. 14a). However, the error distributions of the trinocular measurements are more skewed. These findings suggest that the choice of edge localisation method and the number of cameras used can have a significant impact on the accuracy of length measurements, particularly when dealing with images that are not subjected to high levels of noise.

3.3. *Displacement test*

To further validate the measurement quality results, we employ the laser interferometer described in Section 2.1 to obtain reference displacement measurements. The laser interferometer measurements

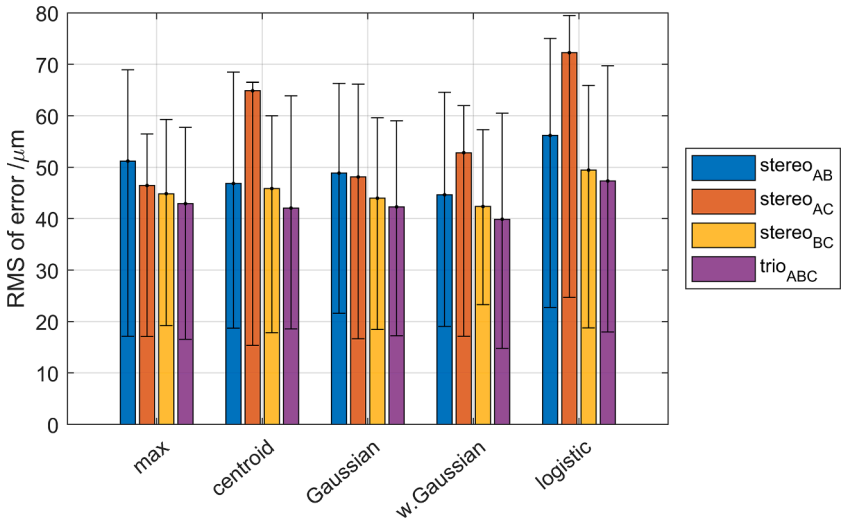

Fig. 15. Root mean square (RMS) of displacement errors evaluated for binocular and trinocular CMSs for 25 mm nominal displacements. Error bars show the minimum and maximum errors.

are not influenced by either the measurement artefact or the captured images. The artefact is displaced by nominal displacements of 25 mm and the vision-based displacements, evaluated from the change in sphere coordinate positions, are compared. Using the reference calibrated displacements from the laser interferometer, the displacement error of the vision CMS for different edge localisation methods and camera combinations is given in Fig. 15.

The vertical bars in Fig. 15 indicate the root-mean-square (RMS) of displacement errors while the error bars show the minimum and maximum error values evaluated for each binocular and trinocular camera combinations. The same set of images used for the measurement quality evaluations given in Section 3.2 are used for the displacement test here.

Comparing the trinocular and binocular results in Fig. 15, the improvement in trinocular CMSs agrees with the improvement in length measurement shown in Fig. 14. The RMS error of the trinocular system is lower than the error of the binocular systems.

Fig. 15 shows that trinocular measurements exhibit a consistently lower RMS displacement error, which corroborates the findings presented in Section 3.2. Unlike the length measurements, the weighted Gaussian edge localisation method performs comparably to the maximum gradient, gradient centroid and Gaussian edge localisation methods. The discrepancy in performance between the displacement and length measurements can be attributed to the fact that the measured length scales in the two measurements vary. Despite having the lowest error for the robustness test presented in Fig. 9, the logistic edge localisation method exhibits the highest error in Fig. 15. As mentioned earlier in Section 3.1, the performance of the logistic edge localisation method deteriorates when actual images are used.

4. Conclusion

For applications in coordinate metrology, this paper investigates vision algorithms used to sample, localise and model ellipse image features for a multi-sphere artefact measurement. The multi-sphere artefact spatially encodes the sphere diameters and spacings to enable spherical feature identification and measurement. From the localised image features of the artefact, we derived the metric 3D coordinates and size of the artefact spheres. A sphere identification algorithm is proposed using the spatial relationship of the artefact spheres from multi-view images. The performance of sphere size and coordinate measurements are investigated using a contact CMS and a laser interferometer.

Amongst the methods used for image localisation of ellipse edges, gradient-based centroid and Gaussian methods are found to be computationally efficient and robust when the proposed gradient cut-off techniques are applied. In conjunction with the edge localisation methods, the proposed foci-based geometric ellipse model is found to be approximately ten times faster than the orthogonal distance-based geometric model for fitting the ellipse edge points. Moreover, at the improved speed, the foci-based model performs comparably to the orthogonal model in the presence of noise and other systematic errors.

Using the proposed heteroscedastic FBG ellipse model and Gaussian-based or centroid-based edge localisation method, sphere size errors less than 25 μm and sphere-to-sphere length errors less than 100 μm are achievable. The heteroscedastic FBG model is also shown to improve the robustness of homoscedastic FBG model by up to a factor of four. The provided results show that the improved sphere localisation and detection models improves the quality of coordinate measurements. Future work will perform complete acceptance and verification tests to determine the maximum permissible error of the measurement system.

Declaration of Competing Interest

The authors declare that they have no known competing financial interests or personal relationships that could have appeared to influence the work reported in this paper.

Data availability

Data used is access through the cited doi. We uploaded the data through our university and are available to every one (http://doi.org/10.17639/nott.7284).

Acknowledgements

This work is funded by the Engineering and Physical Sciences Research Council (EPSRC) under grant number: EP/T023805/1—High-accuracy robotic system for precise object manipulation (HARISOM).

Supplementary materials

Supplementary material associated with this article can be found, in the online version, at doi:10.1016/j.optlaseng.2023.107885.

Appendix A. Solution of edge point localisation methods

A.1 Logistic edge spread function model

From the logistic function given in Eq. (1),

$$\boldsymbol{f}_h(\boldsymbol{x}) = \frac{y_h}{1 + e^{-\frac{(x-\mu_h)}{s_h}}} + d_h,$$

we designate the logistic parameters as $\boldsymbol{\Psi} = [\mu_h, s_h, y_h, d_h]$ and determine the values of the parameters for which $\boldsymbol{x}$ and $\boldsymbol{f}_h$ closely fit the observed ESF data.

Given ESF data $(x_i, y_i)|_{i=1,2\ldots n}$ of size n, consider $f_h(x_i, \boldsymbol{\Psi})$ as the logistic function value at x_i for the unknown values of $\boldsymbol{\Psi}$. We determine $\boldsymbol{\Psi}$ by solving

$$\min_{\boldsymbol{\Psi}} \left(\sum_{i=1}^{n} (y_i - f_h(x_i, \boldsymbol{\Psi}))^2 \right), \tag{A1}$$

where iterations of $\boldsymbol{\Psi}$ are evaluated, starting with the initial parameter value $\boldsymbol{\Psi} = \boldsymbol{\Psi}_0$. For improved stability, the minimisation problem given in Equation $(A1)$ is solved for a constraint $\boldsymbol{\Psi}$, such that $\boldsymbol{\Psi}_l < \boldsymbol{\Psi}_0 < \boldsymbol{\Psi}_u$. $\boldsymbol{\Psi}_l$ and $\boldsymbol{\Psi}_u$ are the respective lower and upper bounds of the values of the logistic parameters prescribed for the expected ESFs. Equation $(A1)$ is implemented using the "*lsqcurvefit*" function of the MATLAB optimisation toolbox.

A.2 Gaussian line spread function model

The Gaussian edge spread model is simplified by taking the natural logarithm of Eq. (2),

$$\ln\left(f_g(x)\right) = \ln\left(y_0 e^{-\frac{(x-\mu)^2}{2\sigma^2}}\right),$$

which can be expanded and grouped into

$$ln\left(f_g(x)\right) = \ln(y_0) - \frac{\mu^2}{2\sigma^2} + \frac{2\mu x}{2\sigma^2} - \frac{x^2}{2\sigma^2}. \tag{A2}$$

Equation $(A2)$ is observed to be quadratic in terms of x and is simplified as

$$\ln\left(f_g(x)\right) = a + bx + cx^2,$$

where $a = \ln(y_0) - \frac{\mu^2}{2\sigma^2}$, $b = \frac{2\mu}{2\sigma^2}$ and $c = -\frac{1}{2\sigma^2}$.

Given the LSF data $(x_i, y_i)|_{i=1,2\ldots n}$ of size n, obtained by sampling the edge profile of a spherical feature, the following objective function is minimised to find parameters a, b and c:

$$\delta(a,b,c) = \sum_{i=1}^{n} \left(\ln(y_i) - \ln\left(f_g(x)\right)\right)^2 = \sum_{i=1}^{n} \left(\ln(y_i) - \left(a + bx_i + cx_i^2\right)\right)^2.$$

The derivative of $\delta(a,b,c)$ with respect to $[a,b,c]$ yields the following linear systems of equations

$$\nabla\delta = \begin{bmatrix} \frac{\partial\delta}{\partial a} \\ \frac{\partial\delta}{\partial b} \\ \frac{\partial\delta}{\partial c} \end{bmatrix} = \begin{bmatrix} n & \sum_{i=1}^{n} x_i & \sum_{i=1}^{n} x_i^2 \\ \sum_{i=1}^{n} x_i & \sum_{i=1}^{n} x_i^2 & \sum_{i=1}^{n} x_i^3 \\ \sum_{i=1}^{n} x_i^2 & \sum_{i=1}^{n} x_i^3 & \sum_{i=1}^{n} x_i^4 \end{bmatrix} \cdot \begin{bmatrix} a \\ b \\ c \end{bmatrix} - \begin{bmatrix} \sum_{i=1}^{n} \ln(y_i) \\ \sum_{i=1}^{n} x_i \ln(y_i) \\ \sum_{i=1}^{n} x_i^2 \ln(y_i) \end{bmatrix}. \tag{A3}$$

The global minima of the function δ is obtained when $\nabla\delta = 0$, leading to the linear problem:

$\boldsymbol{A\eta} = \boldsymbol{b}$, where $\boldsymbol{\eta} = [a,b,c]^{\mathrm{T}}$ and $\boldsymbol{A}$ and $\boldsymbol{b}$ are the respective substitutions of the matrix and vector terms in Equation (A3) corresponding to $\nabla\delta = \boldsymbol{A}\cdot\boldsymbol{\eta} - \boldsymbol{b}$.

The unknown parameters contained in $\boldsymbol{\eta}$ are solved linearly using lower-upper (LU) factorisation $\boldsymbol{\eta} = \boldsymbol{A}^{-1}\boldsymbol{b}$. The values of μ, σ and y_0 are then determined from the calculated parameters $\boldsymbol{\eta}$.

In the presence of additive random noise, the contribution of the noise to the expectation of δ is proportional to $\frac{1}{y_i^2}$ [61]. Therefore, when $|y_i|$ is large compared to the scale of the noise, the influence of the noise is negligible but, when $|y_i|$ is relatively small, δ is affected by noise. A weighted Gaussian objective function, defined as $\delta_w(a,b,c) = y_i^2\delta(a,b,c)$, reduces the sensitivity of the Gaussian objective function to random noise. Gradient of $\delta_w(a,b,c)$, in a similar way to Equation $(A3)$, is derived and the parameter values μ, σ and y_0 are obtained for the weighted Gaussian line spread function model.

Appendix B. Gradient of FBG objective function

The solution of the FBG ellipse fitting problem involves using the gradient of the FBG objective function, given by Equation (6), to determine the gradient decent direction when minimising the objective function. The FBG error function in Equation (6) depends on the ellipse parameters $\boldsymbol{\Lambda} = [a, c_{u1}, c_{v1}, c_{u2}, c_{v2}]$, where the value of the spread standard deviation σ_i is updated for every iteration of $\boldsymbol{\Lambda}$ using Equation (5). For $\boldsymbol{x}_i = [x_u, x_v]^\top$, $\boldsymbol{c}_1 = [c_{1u}, c_{1v}]$ and $\boldsymbol{c}_2 = [c_{2u}, c_{2v}]$, to the simplify gradient computation, define $h = \sqrt{(c_{1u} - c_{2u})^2 + (c_{1v} - c_{2v})^2}$, $h_1 = \sqrt{(x_u - c_{1u})^2 + (x_v - c_{1v})^2}$ and $h_2 = \sqrt{(x_u - c_{2u})^2 + (x_v - c_{2v})^2}$.

From the above definitions, $\cos(\psi_i)$ from Equation (6) can be expressed as

$\cos(\psi_i) = \frac{h_1^2 + h_2^2 - h^2}{2h_1h_2}$.

The error function in Equation (6) can now be expressed as

$\delta_{FBG}(a, c_{u1}, c_{v1}, c_{u2}, c_{v2}) = \frac{1}{\mathrm{n}} \sum_i \frac{1}{\sigma_i^2} \frac{2h_1h_2(h_1 + h_2 - 2a)^2}{\gamma(h_1^2 + h_2^2 - h^2) + 2h_1h_2}$.

For the gradient computations, we define $g(a, c_{u1}, c_{v1}, c_{u2}, c_{v2})$ as

$$g(a, c_{u1}, c_{v1}, c_{u2}, c_{v2}) = \frac{2h_1h_2(h_1 + h_2 - 2a)^2}{\gamma\left(h_1^2 + h_2^2 - h^2\right) + 2h_1h_2},$$

such that

$$\delta_{FBG} = \frac{1}{\mathrm{n}} \sum_i \frac{1}{\sigma_i^2} g(a, c_{u1}, c_{v1}, c_{u2}, c_{v2}).$$

We can then express the gradients of $g(a, c_{u1}, c_{v1}, c_{u2}, c_{v2})$ as

$$\frac{\partial g}{\partial a} = \frac{-8h_1h_2(h_1 + h_2 - 2a)}{\gamma\left(h_1^2 + h_2^2 - h^2\right) + 2h_1h_2}$$

$$\frac{\partial g}{\partial c_{1u}} = \frac{(-2h_2h_{1u}(h_1 + h_2 - 2a))((h_1 + h_2 - 2a) + 2h_1)}{h_1\left(\gamma\left(h_1^2 + h_2^2 - h^2\right) + 2h_1h_2\right)} + \frac{4h_2(h_1 + h_2 - 2a)^2(\gamma h_1(h_{1u} + h_u) + h_2h_{1u})}{\left(\gamma\left(h_1^2 + h_2^2 - h^2\right) + 2h_1h_2\right)^2}$$

$$\frac{\partial g}{\partial c_{1v}} = \frac{(-2h_2h_{1v}(h_1 + h_2 - 2a))((h_1 + h_2 - 2a) + 2h_1)}{h_1\left(\gamma\left(h_1^2 + h_2^2 - h^2\right) + 2h_1h_2\right)} + \frac{4h_2(h_1 + h_2 - 2a)^2(\gamma h_1(h_{1v} + h_v) + h_2h_{1v})}{\left(\gamma\left(h_1^2 + h_2^2 - h^2\right) + 2h_1h_2\right)^2}$$

$$\frac{\partial g}{\partial c_{2u}} = \frac{(-2h_1h_{2u}(h_1 + h_2 - 2a))((h_1 + h_2 - 2a) + 2h_2)}{h_2\left(\gamma\left(h_1^2 + h_2^2 - h^2\right) + 2h_1h_2\right)} + \frac{4h_1(h_1 + h_2 - 2a)^2(\gamma h_2(h_{2u} - h_u) + h_1h_{2u})}{\left(\gamma\left(h_1^2 + h_2^2 - h^2\right) + 2h_1h_2\right)^2}$$

$\frac{\partial g}{\partial c_{2v}} = \frac{(-2h_1h_{2v}(h_1 + h_2 - 2a))((h_1 + h_2 - 2a) + 2h_2)}{h_2(\gamma(h_1^2 + h_2^2 - h^2) + 2h_1h_2)} + \frac{4h_1(h_1 + h_2 - 2a)^2(\gamma h_2(h_{2v} - h_v) + h_1h_{2v})}{(\gamma(h_1^2 + h_2^2 - h^2) + 2h_1h_2)^2}$.

Finally, the gradient of the error function is given by

$$\nabla\delta_{\mathrm{FBG}} = \begin{bmatrix} \frac{\partial \delta_{FBG}}{\partial a} \\ \frac{\partial \delta_{FBG}}{\partial c_{1u}} \\ \frac{\partial \delta_{FBG}}{\partial c_{1v}} \\ \frac{\partial \delta_{FBG}}{\partial c_{2u}} \\ \frac{\partial \delta_{FBG}}{\partial c_{2v}} \end{bmatrix} = \begin{bmatrix} \frac{1}{\mathrm{n}} \sum_i \frac{1}{\sigma_i^2} \frac{\partial g}{\partial a} \\ \frac{1}{\mathrm{n}} \sum_i \frac{1}{\sigma_i^2} \frac{\partial g}{\partial c_{1u}} \\ \frac{1}{\mathrm{n}} \sum_i \frac{1}{\sigma_i^2} \frac{\partial g}{\partial c_{1v}} \\ \frac{1}{\mathrm{n}} \sum_i \frac{1}{\sigma_i^2} \frac{\partial g}{\partial c_{2u}} \\ \frac{1}{\mathrm{n}} \sum_i \frac{1}{\sigma_i^2} \frac{\partial g}{\partial c_{2v}} \end{bmatrix}$$

References

[1] Zhang S. High-speed 3D shape measurement with structured light methods: A review Opt. Lasers Eng 2018;106:119–31. https://doi.org/10.1016/j.optlaseng.2018.02.017.

[2] Zhang G, Yang S, Hu P, Deng H. Advances and Prospects of Vision-Based 3D Shape Measurement Methods. Machines 2022;10:124. https://doi.org/10.3390/machines10020124.

[3] Javaid M, Haleem A, Singh RP, Rab S, Suman R. Exploring impact and features of machine vision for progressive industry 4.0 culture. Sensors Int 2022;3:100132. https://doi.org/10.1016/j.sintl.2021.100132.

[4] Catalucci S, Thompson A, Piano S, Branson DT, Leach R. Optical metrology for digital manufacturing: a review. Int J Adv Manuf Technol 2022;120:4271–90. https://doi.org/10.1007/s00170-022-09084-5.

[5] Alonso V, Dacal-Nieto A, Barreto L, Amaral A, Rivero E. Industry 4.0 implications in machine vision metrology: an overview. Procedia Manuf 2019;41:359–66. https://doi.org/10.1016/j.promfg.2019.09.020.

[6] Catalucci S, Thompson A, Eastwood J, Zhang ZM, Branson Iii DT, Leach R, Piano S. Smart optical coordinate and surface metrology. Meas Sci Technol 2023;34:12001. https://doi.org/10.1088/1361-6501/ac9544.

[7] Villalba-Diez J, Schmidt D, Gevers R, Ordieres-Meré J, Buchwitz M, Wellbrock W. Deep Learning for Industrial Computer Vision Quality Control in the Printing Industry 4.0. Sensors 2019;19:3987. https://doi.org/10.3390/s19183987.

[8] Pérez L, Rodríguez Í, Rodríguez N, Usamentiaga R, García D. Robot Guidance Using Machine Vision Techniques in Industrial Environments: A Comparative Review. Sensors 2016;16:335. https://doi.org/10.3390/s16030335.

[9] Hashmi AW, Mali HS, Meena A, Khilji IA, Hashmi MF, Saffe SN, binti M. Machine vision for the measurement of machining parameters: A review Mater. Today Proc 2022;56:1939–46. https://doi.org/10.1016/j.matpr.2021.11.271.

[10] Penumuru DP, Muthuswamy S, Karumbu P. Identification and classification of materials using machine vision and machine learning in the context of industry 4.0. J Intell Manuf 2020;31:1229–41. https://doi.org/10.1007/s10845-019-01508-6.

[11] Carmignato S, De Chiffre L, Bosse H, Leach RK, Balsamo A, Estler WT. Dimensional artefacts to achieve metrological traceability in advanced manufacturing. CIRP Ann 2020;00:1–24. https://doi.org/10.1016/j.cirp.2020.05.009.

[12] Shi S, Muralikrishnan B, Lee V, Sawyer D. Methods to improve the dimensional measurement accuracy of a motion tracking system. Opt Lasers Eng 2020;130: 106092. https://doi.org/10.1016/j.optlaseng.2020.106092.

[13] Smith ML, Smith LN, Hansen MF. The quiet revolution in machine vision - a state-of-the-art survey paper, including historical review, perspectives, and future directions. Comput Ind 2021;130:103472. https://doi.org/10.1016/j.compind.2021.103472.

[14] Isa MA, Sims-Waterhouse D, Piano S, Leach RK. Volumetric error modelling of a stereo vision system for error correction in photogrammetric three-dimensional coordinate metrology. Precis Eng 2020;64:188–99. https://doi.org/10.1016/j.precisioneng.2020.04.010.

[15] Sims-Waterhouse D, Piano S, Leach R. Verification of micro-scale photogrammetry for smooth three-dimensional object measurement. Meas Sci Technol 2017;28. https://doi.org/10.1088/1361-6501/aa6364.

[16] Gayton G, Isa M, Leach RK. Evaluating parametric uncertainty using non-linear regression in fringe projection. Opt Lasers Eng 2023;162:107377. https://doi.org/10.1016/j.optlaseng.2022.107377.

[17] Peng K, Cao Y, Wu Y, Xiao Y. A new pixel matching method using the modulation of shadow areas in online 3D measurement. Opt Lasers Eng 2013;51:1078–84. https://doi.org/10.1016/j.optlaseng.2013.03.008.

[18] Isa MA, Lazoglu I. Design and analysis of a 3D laser scanner. Measurement 2017; 111:122–33. https://doi.org/10.1016/j.measurement.2017.07.028.

[19] Goda I, Hostis GL, Guerlain P. In-situ non-contact 3D optical deformation measurement of large capacity composite tank based on close-range photogrammetry. Opt Lasers Eng 2019;119:37–55. https://doi.org/10.1016/j.optlaseng.2019.02.006.

[20] Barone S, Paoli A, Razionale AV. Multiple alignments of range maps by active stereo imaging and global marker framing. Opt Lasers Eng 2013;51:116–27. https://doi.org/10.1016/j.optlaseng.2012.09.003.

[21] Zhang X, Song Y, Yang Y, Pan H. Stereo vision based autonomous robot calibration. Rob Auton Syst 2017;93:43–51. https://doi.org/10.1016/j.robot.2017.04.001.

[22] Ye M, Liang J, Li L, Zong Y, Guo J, Tang Z, Ma S, Chen R. Simultaneous measurement of external and internal surface shape and deformation based on photogrammetry and stereo-DIC. Opt Lasers Eng 2022;158:107179. https://doi.org/10.1016/J.OPTLASENG.2022.107179.

[23] Luhmann T, Robson S, Kyle S, Boehm J. Close-Range photogrammetry and 3D imaging (De gruyter). 2013. https://doi.org/10.1515/9783110302783.

[24] ISO 10360. Geometrical product specifications (GPS)—Acceptance and reverification tests for coordinate measuring machines (CMM). Geneva: International Organization for Standardization; 2000.

[25] VDI/VDE 2634 Part 3. Optical 3D-measuring systems - Multiple view systems based on area scanning-Part 3. Berlin: VDI/VDE; 2008.

[26] Kwon YC, Jang JW, Hwang Y, Choi O. Multi-Cue-Based Circle Detection and Its Application to Robust Extrinsic Calibration of RGB-D Cameras. Sensors 2019;19. https://doi.org/10.3390/s19071539.

[27] Thompson A, Southon N. Performance verification for optical co-ordinate metrology. In: Leach R, editor. Advances in optical form and coordinate metrology. IOP Publishing; 2020. p. 205–29.

[28] Nixon MS, Aguado AS. Feature extraction and image processing for computer vision. 2019. https://doi.org/10.1016/C2017-0-02153-5.

[29] Luhmann T. Eccentricity in images of circular and spherical targets and its impact on spatial intersection. Photogramm Rec 2014;29:417–33. https://doi.org/10.1111/phor.12084.

[30] Pongratz M, Mironov K. Accuracy of positioning spherical objects with a stereo camera system. In: Proceedings of the IEEE International Conference on Industrial Technology vol 2015-June. Seville: IEEE; 2015. p. 1608–12. https://doi.org/10.1109/icit.2015.7125326.

[31] Fitzgibbon A, Pilu M, Fisher RB. Direct least square fitting of ellipses. IEEE Trans Pattern Anal Mach Intell 1999;21:476–80. https://doi.org/10.1109/34.765658.

[32] Yu J, Kulkarni SR, Poor HV. Robust ellipse and spheroid fitting. Pattern Recognit Lett 2012;33:492–9. https://doi.org/10.1016/j.patrec.2011.11.025.

[33] Masaoka K, Yamashita T, Nishida Y, Sugawara M. Modified slanted-edge method and multidirectional modulation transfer function estimation. Opt Express 2014; 22:6040–6. https://doi.org/10.1364/OE.22.006040.

[34] Lee SW, Lee SY, Pahk HJ. Precise Edge Detection Method Using Sigmoid Function in Blurry and Noisy Image for TFT-LCD 2D Critical Dimension Measurement. Curr Opt Photonics 2018;2:69–78. https://doi.org/10.3807/COPP.2018.2.1.069.

[35] Feng Y, Tao W, Feng Y, Yin X, Lv N, Zhao H. High-precision width measurement method of laser profile sensor. Sens Rev 2020;40:699–707. https://doi.org/10.1108/sr-06-2019-0154.

[36] Matsuoka R, Maruyama S. Eccentricity on an Image Caused By Projection of a Circle and a Sphere. In: ISPRS Ann. Photogramm. Remote Sens. Spat. Inf. Sci. III–5; 2016. p. 19–26. https://doi.org/10.5194/isprsannals-iii-5-19-2016.

[37] Sims-Waterhouse D, Isa M, Piano S, Leach R. Uncertainty model for a traceable stereo-photogrammetry system. Precis Eng 2020;63. https://doi.org/10.1016/j.precisioneng.2019.12.008.

[38] Qiao G. Advanced Sensor and Target Development to Support Robot Accuracy Degradation Assessment. In: 2019 IEEE 15th International Conference on Automation Science and Engineering (CASE) vol 2019-Augus. IEEE; 2019. p. 54–9. https://doi.org/10.1109/coase.2019.8843200.

[39] Sarmadi H, Munoz-Salinas R, Berbis MA, Medina-Carnicer R. Simultaneous Multi-View Camera Pose Estimation and Object Tracking with Squared Planar Markers. IEEE Access 2019;7:22927–40. https://doi.org/10.1109/ACCESS.2019.2896648.

[40] Pintaric T, Kaufmann H. A rigid-body target design methodology for optical pose-tracking systems. In: Proceedings of the 2008 ACM symposium on Virtual reality software and technology - VRST '08. ACM Press; 2008. https://doi.org/10.1145/1450579.1450594.

[41] Liu B, Zhang F, Qu X. A Method for Improving the Pose Accuracy of a Robot Manipulator Based on Multi-Sensor Combined Measurement and Data Fusion. Sensors 2015;15:7933–52. https://doi.org/10.3390/s150407933.

[42] Qiao G. Advanced sensor and target development to support robot accuracy degradation assessment. In: IEEE International Conference on Automation Science and Engineering. 2019-Augus. IEEE; 2019. p. 54–9. https://doi.org/10.1109/COASE.2019.8843200.

[43] Filion A, Joubair A, Tahan AS, Bonev IA. Robot calibration using a portable photogrammetry system. Robot Comput Integr Manuf 2018;49:1339–51. https://doi.org/10.1016/j.rcim.2017.05.004.

[44] Luhmann T. Precision potential of photogrammetric 6DOF pose estimation with a single camera. ISPRS J Photogramm Remote Sens 2009;64:275–84. https://doi.org/10.1016/j.isprsjprs.2009.01.002.

[45] Boby RA. Identification of elasto-static parameters of an industrial robot using monocular camera Robot. Comput Integr Manuf 2022;74:102276. https://doi.org/10.1016/j.rcim.2021.102276.

[46] Wang J, Tao B, Gong Z, Yu S, Yin Z. A Mobile Robotic Measurement System for Large-scale Complex Components Based on Optical Scanning and Visual Tracking Robot. Comput Integr Manuf 2021;67:102010. https://doi.org/10.1016/j.rcim.2020.102010.

[47] Schmidt J, Grandi F, Peruzzini M, Raffaeli R, Pellicciari M. Novel Robotic Cell Architecture for Zero Defect Intelligent Deburring. Procedia Manuf 2020;51:140–7. https://doi.org/10.1016/j.promfg.2020.10.021.

[48] Lu R, Shao M. Sphere-based calibration method for trinocular vision sensor. Opt Lasers Eng 2017;90:119–27. https://doi.org/10.1016/j.optlaseng.2016.10.004.

[49] Lloyd R, Mccloskey S. Recognition of 3D package shapes for single camera metrology. In: IEEE Winter Conference on Applications of Computer Vision. IEEE; 2014. https://doi.org/10.1109/wacv.2014.6836113.

[50] Sieberth T, Wackrow R, Chandler J. Influence of blur on feature matching and a geometric approach for photogrammetric deblurring. In: ISPRS - Int. Arch. Photogramm. Remote Sens. Spat. Inf. Sci. XL–3; 2014. p. 321–6. https://doi.org/10.5194/isprsarchives-XL-3-321-2014.

[51] Isa MA, Piano S, Leach R. Laser Triangulation. In: Leach R, editor. Advances in optical form and coordinate metrology. IOP Publishing; 2020.

[52] Garcia-Salguero M, Gonzalez-Jimenez J. Certifiable algorithms for the two-view planar triangulation problem. Comput Vis Image Underst 2022;225:103570. https://doi.org/10.1016/J.CVIU.2022.103570.

[53] Leach R. Advances in optical form and coordinate metrology. 2020. https://doi.org/10.1088/978-0-7503-2524-0.

[54] Di Leo G, Liguori C, Pietrosanto A, Sommella P. A vision system for the online quality monitoring of industrial manufacturing. Opt Lasers Eng 2017;89:162–8. https://doi.org/10.1016/j.optlaseng.2016.05.007.

[55] Isa M, Khanesar M, Leach R, Branson D, Piano S. Trinocular vision system for pose determination. In: Proc. ASPE (Bellevue); 2022. p. 277–82.

[56] Wong KYK, Zhang G, Chen Z. A stratified approach for camera calibration using spheres. IEEE Trans Image Process 2011;20:305–16. https://doi.org/10.1109/TIP.2010.2063035.

[57] Atherton TJ, Kerbyson DJ. Size invariant circle detection. Image Vis Comput 1999; 17:795–803. https://doi.org/10.1016/s0262-8856(98)00160-7.

[58] Vacavant A. A Novel Definition of Robustness for Image Processing Algorithms. Reproducible research in pattern recognition. Springer International Publishing; 2017. p. 75–87. https://doi.org/10.1007/978-3-319-56414-2_6.

[59] ISO 12233:2017. Photography — electronic still picture imaging — resolution and spatial frequency responses. 2017.

[60] Caruana RA, Searle RB, Heller T, Shupack SI. Fast algorithm for the resolution of spectra. Anal Chem 1986;58:1162–7. https://doi.org/10.1021/ac00297a041.

[61] Guo H. A Simple Algorithm for Fitting a Gaussian Function [DSP Tips and Tricks]. IEEE Signal Process Mag 2011;28:134–7. https://doi.org/10.1109/MSP.2011.941846.

[62] Hughes GB, Chraibi M. Calculating ellipse overlap areas. Comput Vis Sci 2012;15: 291–301. https://doi.org/10.1007/S00791-013-0214-3.

[63] Sugito Prahuama A, Ispriyanti D, Mustafid. Non-Poisson queue with normal logistic distribution (case study in Semarang automatic toll gate). J Phys Conf Ser 2020; 1524:0–7. https://doi.org/10.1088/1742-6596/1524/1/012138.

[64] Zhang Z. A Flexible New Technique for Camera Calibration. IEEE Trans Pattern Anal Mach Intell 2000;22:1330–4.

[65] Hartley R, Zisserman A. Multiple view geometry in computer vision. Cambridge University Press; 2003.

[66] Bukhari F, Dailey MN. Automatic radial distortion estimation from a single image. J Math Imaging Vis 2013;45:31–45. https://doi.org/10.1007/S10851-012-0342-2.

[67] Brown DC. Close-range camera calibration. Photogramm Eng 1971;37:855–66.

[68] Drap P, Lefèvre J. An exact formula for calculating inverse radial lens distortions. Sensors 2016;16:807. https://doi.org/10.3390/s16060807.

[69] He D, Liu X, Peng X, Ding Y, Gao BZ. Eccentricity error identification and compensation for high-accuracy 3D optical measurement. Meas Sci Technol 2013: 24. https://doi.org/10.1088/0957-0233/24/7/075402.
[70] Wilson RJ. Introduction to graph theory. Pearson; 2010.
[71] Meer P. From a Robust Hierarchy to a Hierarchy of Robustness. In: Davis L S, editor. BT - Foundations of image understanding. Boston, MA: Springer US; 2001. p. 323–47. https://doi.org/10.1007/978-1-4615-1529-6_11.
[72] Vacavant A. A Novel Definition of Robustness for Image Processing Algorithms. BT - Reproducible Research in pattern recognition reproducible research in pattern recognition. 2017. p. 75–87. Cham.
[73] Huang C, Zeng L. Robust image segmentation using local robust statistics and correntropy-based K-means clustering. Opt Lasers Eng 2015;66:187–203. https://doi.org/10.1016/j.optlaseng.2014.09.005.
[74] Isa MA. MultiVision: sphere image simulator. 2023. https://doi.org/10.5281/zenodo.7661305.
[75] Isa MA. Vision and laser-interferometry metrology dataset of a spatially encoded target. 2023. https://doi.org/10.17639/NOTT.7284.